Ultrafast THz optical modulation with 2D-material-based device

Eudokia Kyriakou

Thesis

For the degree of Master of Science

Supervisor: prof. Stelios Tzortzakis

Co-supervisors: prof. Maria Kafesaki, prof. George Kioseoglou

Heraklion, Crete,

Acknowledgments

I would like to thank all the people that supported me during my Master of Science at the department of Materials science and technology of the University of Crete and helped me to successfully complete this work.

Foremost, I would like to express my sincere gratitude to my advisor Prof. Stelios Tzortzakis for the continuous support during the master study and research. Without his guidance and persistent help this dissertation would not have been possible.

I would also like to thank Prof. Maria Kafesaki and Prof. George Kioseoglou for being members in my master committee.

Furthermore, I would like to especially thank my labmates in UNIS Group, Tasos Koulouklidis and Christina Daskalaki for their help and support inside the lab and their guidance during the experiments that presented in my thesis. I would also like to thank Michalis Loulakis for his guidance during my first training in the lab.

I would also like to thank my friends for the great moments we had outside the scientific environment.

Last but not least, I would like to thank my parents John and Eirini and my brothers Manoli and Ilia. They have been always there relying on me and constantly providing their support in any difficulty.

Abstract

Terahertz (THz) radiation technology aims to bridge the realms of electronics and photonics, and therefore it attracts increasing attention over the last two decades. A developing field of applications is that of THz wireless communication systems, particularly within the landscape of the fast-emerging 5G and 6G technologies, where THz waves promise increased bandwidths for the data demanding systems. Therefore, there is a constantly growing demand for efficient modulators that will operate at THz frequencies, with compact size. Under this prism, two-dimensional (2D) materials such as graphene, hold great promise and have sparked widespread interest in the photonics community due to its unique structure and its unprecedented optoelectronic properties

In this master thesis, graphene is investigated as an efficient non-linear material that can be incorporated in modulation devices that operate at THz frequencies. An electrically gate-tuned graphene-based Salisbury screen device is investigated, which consists of a graphene layer, placed on an ionic liquid substrate, back-plated by a metallic back- reflector. We demonstrate that the absorption and phase characteristics of the device can be self-modulated when the intensity of the incident THz field is high enough to drive the graphene layer in the non-linear regime. An amplitude modulation of more than three orders of magnitude in the resonant absorption of our device, and an absolute phase modulation of 130^{o} when the THz field strength increases from 102 to 654 kV/cm is demonstrated. The origin of this nonlinear response is explained by the graphene hot carriers' dynamics. Beyond telecommunications, such devices could find applications in future dynamically modulated flat optics devices, as well as for THz beam spatio-temporal modulation.

Table of contents

1. Introduction

1.1. Basics of Terahertz science

1.1.1 Definition and properties of THz radiation

The electromagnetic spectrum (EM) includes groups of frequencies that are categorized in microwaves, visible light, infrared radiation, ultraviolet radiation, X-rays, and Gamma rays[1]. Higher than the microwave and lower than the infrared frequencies, a group called **terahertz (THz) radiation** exists (see Figure 1). The THz frequency range is typically between 0.1 THz and 30 THz, corresponding to a wavelength range from 3 mm to 10 μm, photon energy from 0.4 meV to 120 meV and to an equivalent black body radiation with temperatures between 4 K to 1200 K[2]. This part of the electromagnetic spectrum has not been well explored due to the lack of practical efficient sources and sensitive detectors. The term "THz gap"[3] resulted from the limits of the electron velocities which prevent electronic devices to operate above a few hundred GHz, and from thermal energies that limit the smallest electronic transitions useful for lasing, preventing solid-state lasers to operate below a few hundred THz.

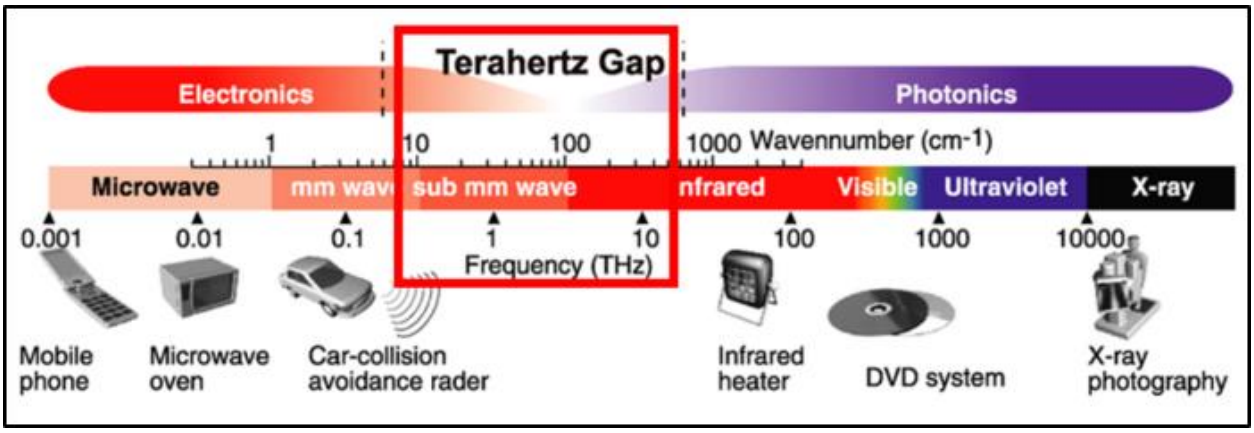

Figure 1: Diagram of the electromagnetic spectrum, showing the location of terahertz (THz) radiation [2].

THz waves are a unique tool for research in several scientific fields due to the interesting properties they have[4]. First of all, THz radiation is sensitive and selective to the nature of the materials it passes through. Many substances show particular spectral characteristics, called fingerprinting by analyzing the frequency dependence of the transmitted THz power. Spectral fingerprints are essential in the process of identifying the chemicals in an unknown target[5]. Furthermore, molecular rotations, low frequency bond vibrations and crystalline phonon vibrations are present in this frequency range[6,7].

Secondly, one of the most valuable properties of terahertz radiation is its ability to pass through a wide range of substances, thus making it possible to 'see' through many materials such as paper, fabrics, plastics, silicon and so on. These materials are transparent at THz frequencies because THz waves are less affected by Mie scattering due to their long wavelengths[8]. In addition, metals are highly reflective due to their high electrical conductivities, that enables us to detect objects that are concealed under various surfaces. Thus, THz radiation can be used in industrial control such as non-destructive testing and security screening at airports.

Furthermore, contrary to X-ray photons that carry high energy (≈keV), which is sufficient to ionize biological tissues, a THz photon is significantly weaker (1 THz ≈ 4.1 meV) and thus THz radiation is harmless in biological tissues. As a result, THz waves are considered safe for both the samples and operator. Moreover, THz radiation is strongly absorbed by water since it can excite rotational modes in water molecules, preventing it from penetrating the human body like microwaves can. The later allows the use of THz radiation for imaging applications (e.g., medical and biological) but only for limited penetration depth (see Figure 2).

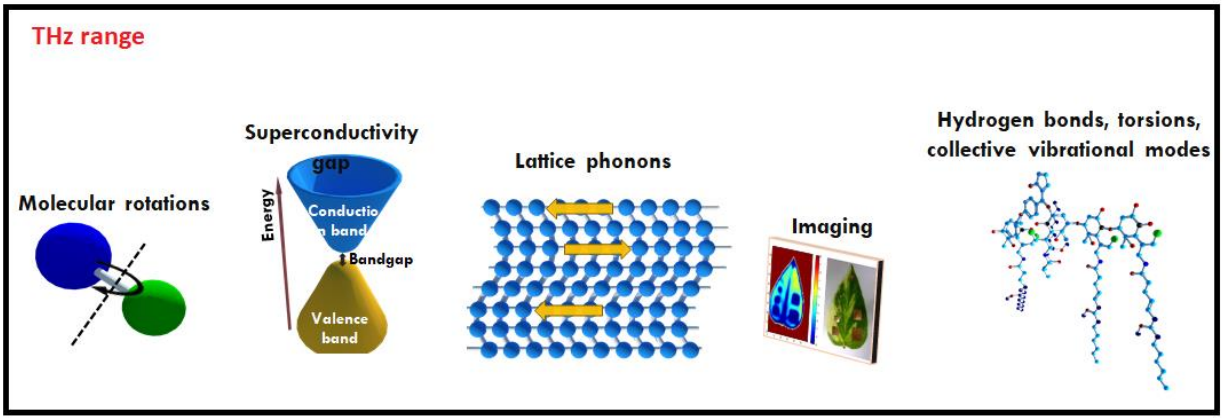

Figure 2: Schematic representation of physical phenomena in THz range.

Especially interesting for researchers is the possibility to use terahertz radiation to investigate numerous solid-state phenomena such as phonon modes of semiconductors and crystals and the band gaps of superconductors[8]. Finally, the ultrashort width of the THz radiation pulses allows for measurements (e.g., thickness, density, defect location) on difficult to probe materials (e.g., foam). Since THz pulses are detected by sampling measurement of the electric field which allows an access to the amplitude and the phase of the radiation absorption and dispersion spectroscopy of many materials can be performed, giving us also chemical and structural information.

1.2 Application of Terahertz radiation

The unique properties of terahertz waves have been exploited in a variety of imaging and sensing applications. These applications of terahertz radiation are applied in a plethora of fields such as communication, astronomy, security, dentistry, pharmacy, quality assurance, medicine and art conservation[9] (see Fig.3).

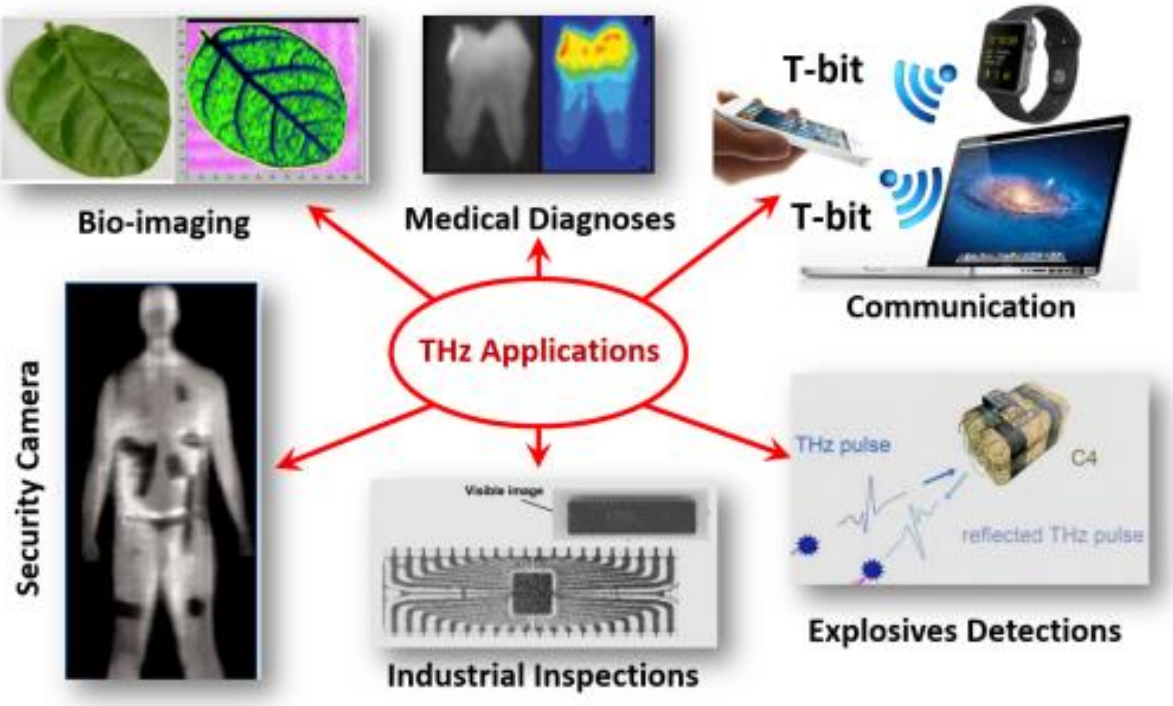

Figure 3: THz imaging and spectroscopy applications.

Broadband THz time - domain spectroscopy (THz-TDS) is a useful and non-invasive tool because THz waves have the ability to characterize the molecular structure of many substances. Especially, in food industry numerous studies have demonstrated the detection of antibiotic residues in food matrices, the detection of pesticides in food powders or the spectroscopic characterization of various products[10].

Furthermore, THz science has been successfully applied to the field of art conservation and cultural heritage[11]. The non-invasive and non-destructive nature of THz imaging and spectroscopy can provide information about the materials below layers of the paint without the need of taking sample from the object. Apart from using THz waves for non-invasive imaging, THz spectroscopy plays a vital role for the analysis of various materials in cultural heritage. Specifically, it can be used to identify pigments and binders that exhibit characteristic fingerprints in the THz frequency range. These two characteristics can give the opportunity to recognize the materials that are used in paintings alone or in combination with pigments and binders (see Figure 4).

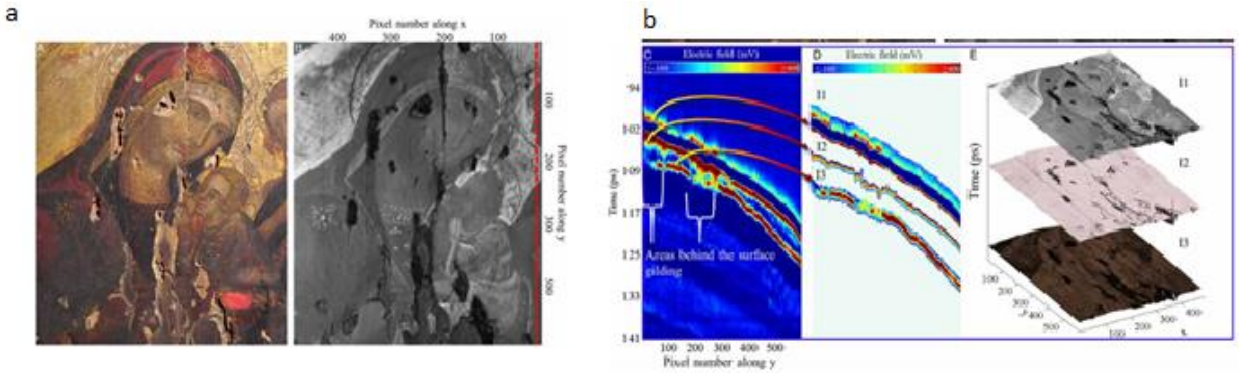

Figure 4: a) A painting in visible and THz image, b) THz images of the different layers of the painting[11]

Another research field of the THz technology is security screening. THz radiation can penetrate plastics and fabrics and thus it can be used in surveillance applications, such as security screening to uncover concealed weapons on a person remotely[12]. Many materials have unique spectral fingerprints in the terahertz range. This offers the possibility to combine spectral identification with imaging[13]. At airports or other security places dangerous non-metallic substances like ceramic knifes or plastic explosives now can be detected with terahertz beams through clothes[14,15] as illustrated in Figure 5.

Figure 5: Terahertz image of man with hidden knife[12]

Another fertile area for the THz science is the medical science since terahertz radiation can penetrate several millimeters of tissue with low water content (e.g., fatty tissue) and reflect back[16]. Terahertz radiation can also detect differences in water content and density of a tissue. Furthermore, important studies have been made on the diagnosis of cancer. By using THz spectroscopy and imaging, it is possible to distinguish a benign tumor from a malignant one. The contrast between them is attributed to their different hydration levels. However, THz imaging as a diagnostic tool is still in initial stage and the systems based on it, still require significant

improvements and development before they can be accepted as non-invasive diagnostic tools by the medical community.

Finally, the communication technology sector constitutes a large potential market for THz applications[15]. In outer space, the transmission of THz is lossless, so we can achieve long-range communications with very little power. At the same time, compared with the current space optical communication, THz wave has wider beam width, so it is easier to pointing in the long-distance space communication. The utilization of THz science would be of great benefit here by enabling high-performance wireless connections.

1.3 THz generation sources

Historically, the most popular approaches in THz pulsed sources are based on photoconductive antennas and optical rectification techniques. THz radiation can be generated in a photoconductive switch on a semiconductor substrate excited by a femtosecond pulse or in an electro-optic crystal by difference-frequency mixing of the frequency components of a femtosecond laser pulse[17]. In this work, their principles will be briefly reviewed to introduce the basic requirements needed for the THz time-domain spectroscopy (THz-TDS).

1.3.1 Photoconductive Antennas (PCAs)

Photoconductive Antennas (PCAs) were first reported by Auston et al. in 1984 for generation of THz radiation from ultrafast optical pulses. Today, PCAs remain the most widely used source and detector for THz-TDS due to their good performance, low cost, and relative simplicity[18].

A photoconductive antenna consists of two electrodes that are deposited on a semi-insulating semiconductor substrate with a gap between them, as depicted in the following Figure 6. A DC voltage is applied across the electrodes to generate THz pulses. Since the substrate is semi-insulating, electric energy is stored in the gap area.

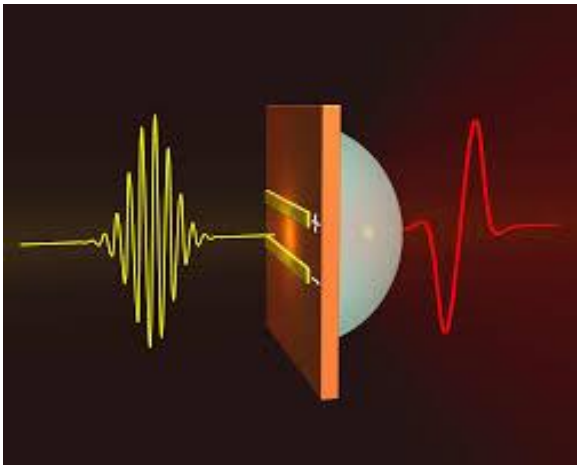

Figure 6: Scheme of photoconductive antenna[18].

The substrate is photoexcited with above bandgap photon energy ultrashort laser pulses at the antenna gap, which moves electrons from the valence to the conduction band of the semiconductor, creating electron-hole pairs. These photocarriers are being accelerated by the applied external DC bias voltage, which creates a transient current gradient and radiates THz pulses. Finally, the THz emitter's electrons return to their original state before the next laser pulse arrives[19]. The charge density decreases on the time scale of carrier lifetime due to trapping of free carriers in the defects. Since electrons have much higher mobility than the holes, the contribution of holes can be ignored in most cases. The current density is then described as:

$$\boldsymbol{J = N(t)e\mu E_b} \quad \textbf{(1)}$$

where N is the density of photocarriers, e is the elementary charge, μ is the mobility of electrons and E_b is the bias electric field. The photocarrier density N is a function of time, whose format is determined by the laser pulse shape and the carrier lifetime. Since the photocurrent varies in time, it generates electromagnetic pulse, whose electric field is approximately:

$$\boldsymbol{E_{THz} = \frac{1}{4\pi\varepsilon_0}\frac{A}{c^2 z}\frac{\partial J(t)}{\partial t} = \frac{Ae}{4\pi\varepsilon_0 c^2 z}\frac{\partial N(t)}{\partial t}\mu E_b} \quad \textbf{(2)}$$

where A is the area in the gap illuminated by the laser light, ε_0 is the vacuum permittivity, c is the speed in vacuum and z is the distance between the field point and the THz source.

Generation of THz radiation through a PCA depends on various factors such as the antenna geometry, the optical pulse duration, the applied bias voltage, along with the properties of the PCA substrate such as bandgap, carrier lifetime and carrier mobility[20]. The typical antenna gap size is of the order of few micrometers. However, this causes a decrease in the effective region where the THz electric field is generated. The applied bias voltage can be increased only up to the damage threshold of the material. To conclude, the energy of the THz pulse comes from the electric field stored across the gap area rather than the optical pulse energy. Since the radiating energy comes from the stored energy in the form of the static bias field, the THz radiation energy increases with the bias and optical fluency[21].

1.3.2 Optical rectification in nonlinear media

Difference frequency mixing or optical rectification (OR) is a popular method for the emission of THz radiation, which is based on the second order nonlinear process in non-centrosymmetric materials [22] (Figure 7). The first attempt to generate THz radiation using OR technique was carried out by Zernike and Berman. It is a process, similar to the linear electro-optic effect, which occurs in crystals that are non-centrosymmetric or it is possible in centrosymmetric

if the symmetry is broken by a strong electric field. Moreover, generation and detection of THz radiation pulses by optical rectification require that the crystals are sufficiently transparent at THz and optical frequencies.

Typically, femtosecond laser pulses are used to generate THz waves via optical rectification. Since a femtosecond pulse is a broadband pulse which contains many frequency components, any two frequency components contribute to the difference-frequency generation, and overall result is the weighted sum of all the contributions[19]. One femtosecond laser pulse is enough to stimulate optical rectification radiation. Mathematically, the polarization P can be expanded into a power series of the electric field:

$$\boldsymbol{P(r,t) = \chi^{1} E(r,t) + \chi^{2}: E(r,t)E(r,t) + \chi^{3}: E(r,t)E(r,t)E(r,t) + \cdots} \quad \textbf{(3)}$$

where χ^{n}(r, t) is the nth-order nonlinear susceptibility tensor. Optical rectification comes from the second term of the above equation. If the incident light is plane wave, the E can be expressed as:

$$\boldsymbol{E(t) = \int_{0}^{+\infty} E(\omega)\, exp(-i\omega t)\, d\omega + c.c} \quad \textbf{(4)}$$

By substituting the equation (3) into equation (4), the polarization for optical rectification is given by:

$$\boldsymbol{P_{OR}^{(2)}(t) = 2\chi^{(2)}: \int_{0}^{\infty}\int_{0}^{\infty} E(\omega_1)E^{*}(\omega_2)\, exp[-i(\omega_1 - \omega_2)t]\, d\omega_1 d\omega_2 = 2\chi^{(2)}: \int_{0}^{\infty}\int_{0}^{\infty} E(\omega + \Omega)E^{*}\, exp[-i\Omega t]\, d\Omega d\omega} \quad \textbf{(5)}$$

where Ω is the frequency difference of the two optical frequency components. The production of the THz radiation relies on the difference frequency generation with the frequency difference to zero[23]. The bandwidth of the THz radiation pulse is determined by difference frequency generation by all frequencies within the bandwidth of the femtosecond laser pulse. In the far field, the radiated field E_r(t) is proportional to the second derivative of the $P_{OR}^{2}(t)$ with respect to time:

$$\boldsymbol{E_r(t) \propto \frac{\partial^2}{\partial^2 t} P_{OR}^{(2)}(t)} \quad \textbf{(6)}$$

The crystal structure affects the susceptibility tensor. Far-field waveform of the radiation can be calculated with a given crystal structure and incident light. Crystal orientation, thickness, absorption and dispersion, diffraction, phase matching and saturation affect the radiation efficiency, waveform and frequency distribution. For a nonlinear process such as THz generation from optical rectification, the most important factor is phase matching. It requires conservation of energy and momentum in the nonlinear process. Only when phase matching is satisfied, all three

waves participating in the optical rectification process can be kept in phase and lead to maximum energy conversion coefficient along the light propagation or phase mismatch leads to a phase walk off while propagating[19]. Finally, the optical rectification is somewhat like a classical electrodynamic emission of radiation by an accelerating/ decelerating charge, except that here the charges are in a bound dipole form and the THz generation depends on the second susceptibility of the nonlinear optical medium [23].

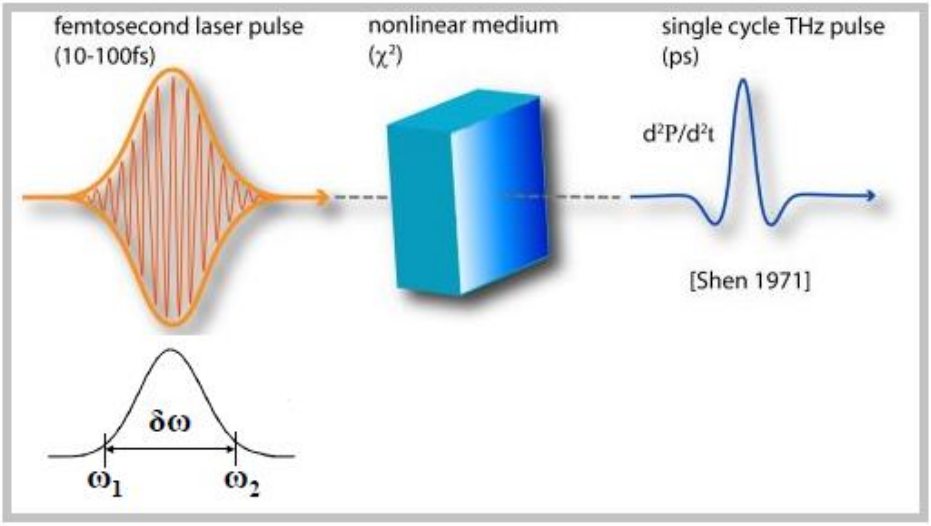

Figure 7: Optical rectification process [24]

1.3.3 Two color filamentation in air

A promising technique to obtain THz pulses with high-field strengths is two-color filamentation of femtosecond lasers in ambient air as is shown in Figure 8. The second harmonic beam is generated by focusing an intense beam through a BBO crystal[25]. Both the fundamental IR pulse (ω) and its second harmonic (2ω) are overlapped, propagated in the same direction and THz emission is the result of a transversal plasma photocurrent produced from a synthesized 2-color asymmetric laser field. The generation of THz pulses through two color photoinduced plasma will be discussed in the following chapter.

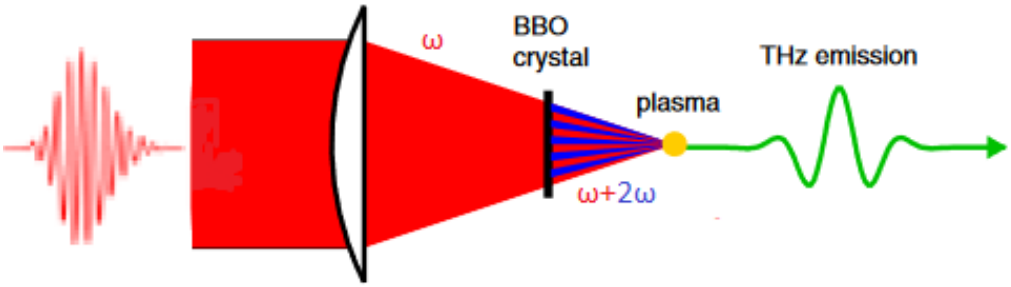

Figure 8: Schematic representation of THz emission through two color filamentation in air[25]

1.4 THz waves detection

THz detection schemes are often classified as being either coherent or incoherent. If they measure the amplitude and phase of the input field, they are coherent, while if they only measure the intensity, they are incoherent[22]. Examples of coherent THz systems are photoconductive antennas (PCA), electro-optic sampling, heterodyne detector and Air Biased Coherent Detection (ABCD) while incoherent THz systems are pyroelectric detectors, bolometers and Golay cells. The latter techniques allow only the signal's amplitude detection and are broadband detection systems with their main advantage being relative operation simplicity without need of adjustment in wide frequency band.

A) Incoherent detection of THz pulses

1.4.1 Heterodyne detector

Heterodyne detection is a method of detecting radiation by non-linear mixing with radiation of a reference frequency. It is commonly used in telecommunications and astronomy for detecting and analyzing signals. The radiation is most commonly either radio waves or light which is mixed with some strong local oscillator wave which is the reference signal. The signal and the local oscillator are superimposed in a mixer. The mixer, which is a (photo)diode, has a non-linear response to the amplitude, that is, at the least part of the output is proportional to the square of the input. A schematic representation of a heterodyne detection system is illustrated in Figure 9 [26].

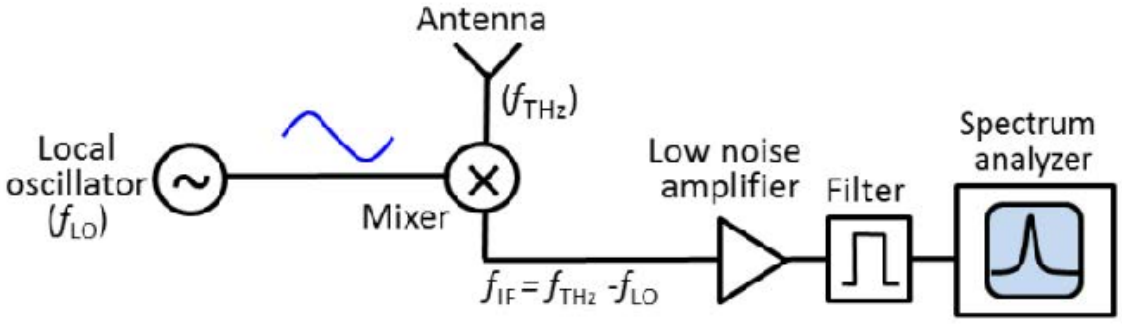

Figure 9: Schematic representation of heterodyne detection[23]

The electric field of the received signal can be represented as:

$$\boldsymbol{E_{sig} cos\,(\omega_{sig} t + \varphi\,)} \qquad \textbf{(7)}$$

and the signal from the local oscillator can be represented as:

$$E_{LO} cos\, \omega_{LO} t \quad (8)$$

The output I of the detector is proportional to the square of the amplitude:

$$I \propto (E_{sig}\, cos\, (\omega_{sig} t + \varphi) + E_{LO} cos\, (\omega_{LO} t))^2 \quad (9)$$

The development of the above equation gives an output which has frequency ($2\omega_{sig}$ and $2\omega_{LO}$) components, a beating component (ω_{sig}-ω_{LO}) as well as constant components. In heterodyne detection, the high frequency components and usually the constant components are filtered out, leaving the intermediate (beat) frequency. The amplitude of this last component is proportional to the amplitude of the signal radiation.

1.4.2 Pyroelectric detector

Pyroelectricity refers to a phenomenon observed in pyroelectric materials, in which a voltage difference is induced across the material when there is a temporal temperature variation. It can be seen as one of the sides of a triangle with three vertices representing the three types of energy present in a material: thermal, mechanical and electrical energy. The side connecting the thermal and electrical energies represents the pyroelectric effect. The schematic of a typical pyroelectric detector is shown in Figure 10. The side connecting the electrical and mechanical energies represents the piezoelectric effect. When there is a temperature change, for example by incident radiation, polarization changes. This change in polarization can be observed as an electrical signal if electrodes are placed on opposite faces of a thin slice of the material to form a capacitor. The sensor will only produce an electrical output signal when a change in temperature occurs. If the temperature is constant, the pyroelectric voltage gradually disappears due to leakage current.

Commonly used pyroelectric materials include triglycine sulphate (TGS), deuterated triglycine sulphate (DTGS), lithium tantalite ($LiTaO_3$) and barium titanate ($BaTiO_3$). Ferromagnetic materials such as $LiTaO_3$ exhibit a large spontaneous electrical polarization varying with temperature[24].

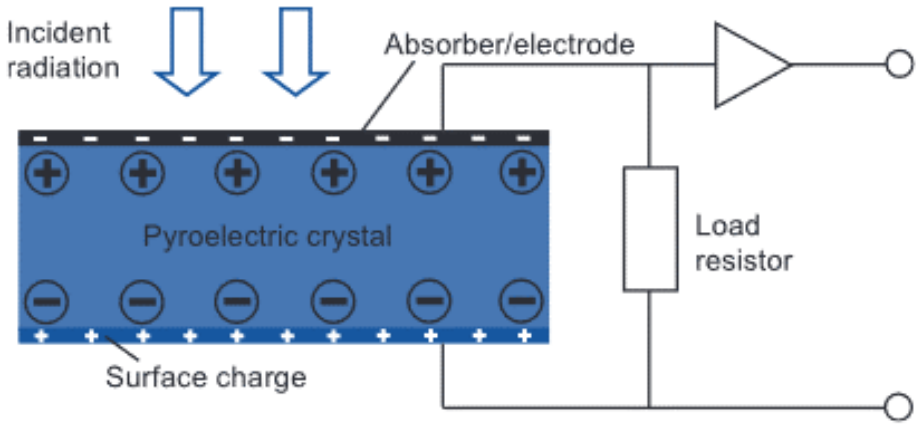

Figure 10: Schematic representation of pyroelectric detection[23]

B) Coherent detection of THz pulses

1.4.3 Photoconductive antennas

Photoconductive antennas (PCAs) excited by ultrashort (femtosecond) laser pulses can be used to detect as well as generate broadband THz radiation. The only major difference is that as a detector, its two electrodes are connected to a current sensor rather than a power supply (Figure 11). By controlling, the time delay between the THz pulse and the optical probe pulse, the electric field across the strip line of the photoconductive antenna at any given time is sampled by the optical probe pulse which serves to generate transient photocarriers in the substrate at that specific time. Since the THz pulses and laser pulses remain for a certain time delay, the photoinduced carriers see a steady field, and are driven by this field to form a current between the two electrodes[27]. The THz field induced current is:

$$\bar{J} = \bar{N} e \mu E(\tau) \quad \textbf{(10)}$$

Here $\bar{N}$ denotes the average electron density and τ is the temporal delay between probe and the THz pulse. By scanning the temporal delay, the THz pulse waveform, as a function of τ is recorded. Typically, the period of the THz oscillation is about one picosecond (ps) and the THz pulses are a sub cycle to a few cycles of oscillation[28]. As shown in the above equation, the detection of THz pulses directly records its field rather than its intensity. The measurement records not only the amplitude, but also the phase information of the THz pulse, which gives access to various parameters.

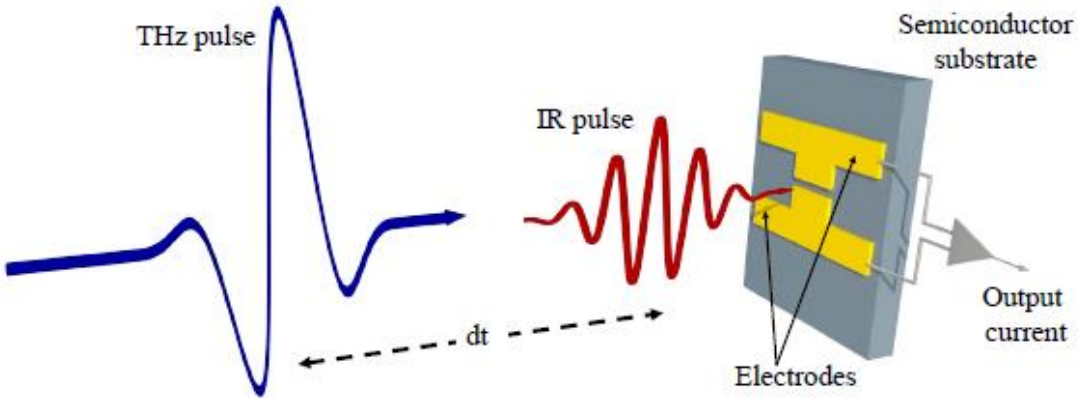

Fig. 11: Terahertz detection using photoconductive antenna[29]

1.4.4 Electro-optic sampling

Another method for the detection of THz radiation is the electro-optic sampling which is based on the Pockels effect, where the THz electric field induces an instantaneous birefringence i.e., difference in the refractive indices along each crystal axis, in an electro-optic crystal (Figure 12)[30]. This varying birefringence leads to a change in polarization of an optical probe pulse which is travelling through the electro-optic medium[27]. This change can be detected after the crystal, using a combination of polarization optics and a pair of photodetectors. More details about this detection method will be given in the following chapter.

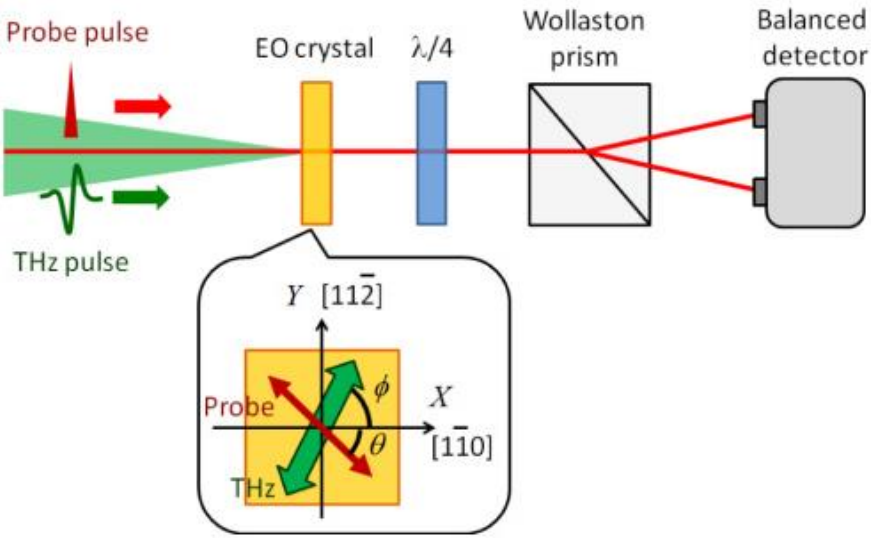

Figure 12: Schematic presentation of EO sampling method [30]

1.4.5 Air Biased Coherent Detection (ABCD)

In this detection technique, the basic principle utilized to sense the pulsed terahertz waves is the measurement of the terahertz field induced optical second harmonic generation (TFISH) through a third order nonlinear process[31]. ABCD is a pump-probe technique and a schematic representation it is depicted in Figure 13. A properly synchronized probe IR pulse at ω frequency is recombined with the THz pulse and are together focused on ambient air between two electrodes that are AC biased, generating a TFISH signal which is then collected by a photomultiplier (PMT). The use of PMT is essential since the 2ω signal generated is extremely weak.

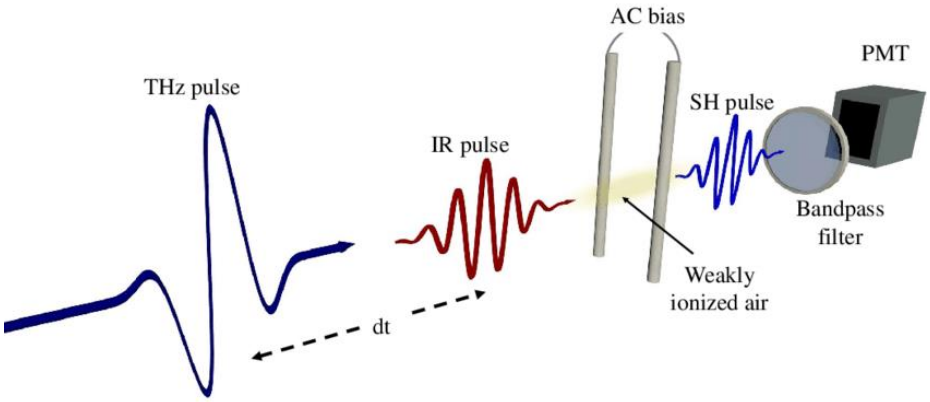

Figure 13: Schematic representation of Air Biased Coherent Detection technique [29]

The AC bias generates an extra second harmonic signal that mixes with terahertz field induced Second harmonic pulse. The second harmonic field generated by the TFISH process can be described as:

$$\boldsymbol{E_{2\omega}^{THz} \propto \chi^{(3)} E_{THz} E_{\omega} E_{\omega} \propto \chi^{(3)} E_{THz} I_{\omega}} \quad \textbf{(11)}$$

where $E_{2\omega}$, E_{ω} and E_{THz} are the electric field amplitudes of 2ω, ω and terahertz waves respectively, $\chi^{(3)}$ is the third order susceptibility of the gas. Since $E_{2\omega} \propto E_{THz} E_{\omega} E_{\omega}$ it follows that the second harmonic field is proportional to the THz electric field. In practice, we measure the intensity or power of the second harmonic but not its electric field. The measured signal in Eq. 11 is incoherent and therefore the phase information is lost, limiting the possible applications of the technique. To realize coherent measurements, a local oscillator at the 2ω frequency $E_{2\omega}^{LO}$ is generated to interfere with the second harmonic induced by the THz field, as expressed by the following equation:

$$\boldsymbol{I_{2\omega} \propto |E_{2\omega}|^2 \left(E_{2\omega}^{THz} + E_{2\omega}^{LO}\right)^2 = E_{2\omega}^{THz^2} + 2E_{2\omega}^{LO} E_{2\omega}^{LO} cos\varphi + E_{2\omega}^{LO^2}} \quad \textbf{(12)}$$

where φ is the phase difference between the $E_{2\omega}^{THz}$ and $E_{2\omega}^{LO}$ which is either 0 or π depends on the direction of the bias field. Terahertz field induced second $E_{2\omega}^{THz}$ and the AC $E_{2\omega}^{LO}$ bias induced second harmonic can be written as:

$$E_{2\omega}^{THz} \propto \chi^{(3)} I_{\omega} E_{THz} \quad (13)$$

$$E_{2\omega}^{LO} \propto \chi^{(3)} I_{\omega} E_{bias} \quad (14)$$

Where E_{bias} is the bias electric field, Using the above equation, Eq. 11 can be written as:

$$I_{2\omega} \propto \left(\chi^{(3)} I_{\omega}\right)^2 (E_{THz})^2 + (E_{bias})^2 \pm 2 E_{bias} E_{THz} \quad (15)$$

Due to the phase modulation of the bias-induced second harmonic, the process can be interpreted in terms of heterodyne detection. Assuming, a constant carrier-envelope phase of the laser pulse, the second harmonic pulses from a frequency comb[31]. The phase modulated pulses have a frequency comb shifted by the modulation frequency and, thus, when the intensity is measured, the detector acts as a mixer, providing the difference frequencies of the combs. Only the cross term is present at the modulation frequency, while the other terms exist only on the even harmonics and, thus lock-in amplification easily isolates the signal proportional to $E_{THz.}$ Under the above description the measured second harmonic intensity will be:

$$I_{2\omega} \propto 4\left[(\chi^{(3)} I_{\omega})\right]^2 E_{bias} E_{THz} \quad (16)$$

And we can see that the intensity of the second harmonic pulse depends now on the electric field the THz pulse allowing it this way to be coherently detected. Finally, ABCD is a coherent and broadband detection scheme but it still has some limitations[29]. Firstly, it is less sensitive than electro optic sampling so the SNR is lower compared to electro optic crystals and secondly, it's detection bandwidth strongly depends on the probe pulse duration.

2. Properties of ultrashort laser pulses

2.1 Self-focusing

Self-focusing is a non-linear optical process induced by the change in refractive index of materials that are exposed to intense electromagnetic radiation. In the presence of a strong laser filed, the refractive index of air, is not only dependent on the frequency of the laser field, but also on its spatio-temporal intensity distribution according to the following relation:

$$\boldsymbol{n = n_0 + n_2 I(r, t)} \tag{17}$$

where n_2 (cm^2/W) is the nonlinear refractive index of the medium and depends on the frequency of the incident wave and the material properties, n_0 is the linear refractive index of the material and I (r, t) is the intensity of the field at a specific point in time and space[32]. Typically, the nonlinear refractive index n_2 is of the order of 10^{-19} cm^2/W in gases and 10^{-16} cm^2/W in amorphous solids and liquids. In a Gaussian laser beam, the central part of the has higher intensity and thus for positive n_2, the central part of the beam experiences a larger refractive index than the edges. This forces the material to act as a positive lens, forcing the beam to self-focus inside the material as depicted in figure 14. This phenomenon occurs when the Kerr lensing effect is significant enough to overcome beam divergence due to diffraction. This is possible only if the power carried by the beam is above a critical value. For Gaussian beam the critical power is expressed as:

$$\boldsymbol{P_{Cr} = \frac{3.77\lambda_0^2}{8\pi n_0 n_2}} \tag{18}$$

Typically, the critical power for an 800 nm laser pulse is about 3.2 GW in air and 4 MW in water.

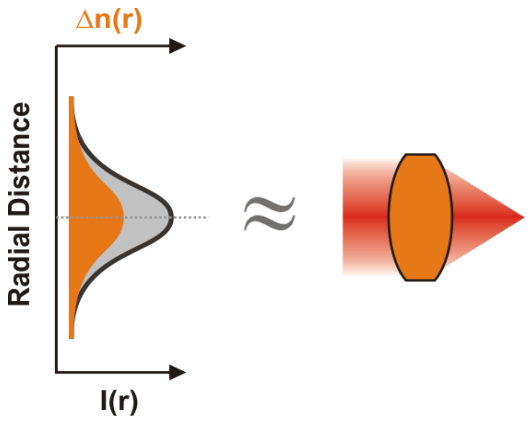

Figure 14: Schematics representation of self-focusing of a Gaussian beam. Black line: Intensity distribution orange: refractive index modulation[29].

2.1.1 Optical field ionization and plasma defocusing

Optical field ionization or photo-ionization is one of the main mechanisms that arrest the beam collapse from self -focusing. When the light field is strong or the intensity is high, photo-ionization can take place through nonlinear mechanisms. In photo-ionization, the energetic electrons in the valence band are promoted to the conduction band depending on the intensity and energy of the incident beam[33]. It can occur by two methods, namely, tunneling and multiphoton ionization as shown in figure 15. Multiphoton ionization (MPI) is the first process to occur and its rate scales as 1^k, where k is the number of simultaneously absorbed photons. For air is approximately equal to 8 at a laser wavelength 800nm. At higher intensities, tunnel ionization occurs where an electron escapes through the barrier deformation formed by the electromagnetic field and the Coulomb potential[34]. In terms of laser intensity, the MPI is responsible for relatively low laser intensities 10^{12} - 10^{13} W/cm^2, whereas tunneling ionization is responsible for intensities 10^{14} W/cm^2 and above.

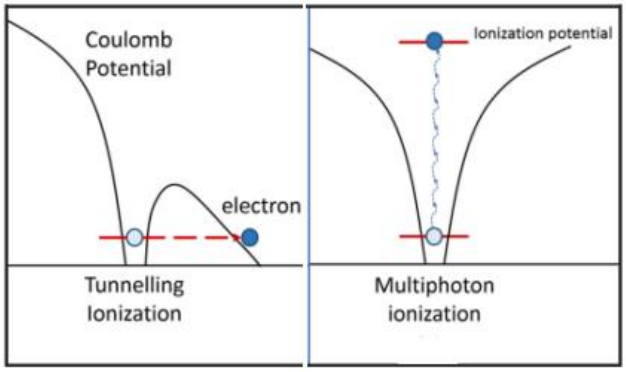

Figure 15: Photo-ionization mechanisms[33]

The direct effect of this plasma formation is a local reduction of refractive index. This effect acts as a negative defocusing lens, preventing the beam from collapsing. The index variation due to the plasma is expressed as:

$$\boldsymbol{n = n_0 - \frac{\rho(r,t)}{2\rho_c}} \quad \textbf{(19)}$$

where ρ is the electron density of the generated plasma and ρ_c the critical plasma density. Plasma defocusing is a higher order nonlinear process than self-focusing, and therefore it will eventually dominate given high enough intensity values. A schematic presentation of plasma defocusing is shown in Figure 16.

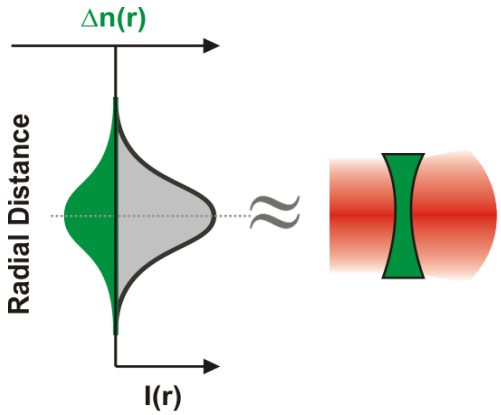

Figure 16: Schematics representation of plasma-defocusing. Black line: Intensity distribution green: refractive index modulation[29]

2.1.2 Filamentation

Numerous non-linear phenomena occur during the propagation of high intensity ultrashort laser pulses in air. An impressive example of these phenomena is the so-called filamentation. It is a highly complex and dynamical physical phenomenon that results from the nonlinear interaction between an intense optical field and the medium through which it propagates. After propagating, a femtosecond laser pulse turns into a white light laser pulse whose transverse pattern shows a central white spot surrounded by colored rings[35]. Linear phenomena such as diffraction and dispersion are acting on the wave packet and given enough power the beam will start self-focus. Self-focusing leads to an increase of the intensity, which will in turn accelerate the self-focusing process. Close to the point of collapse the intensity of the pulse is high enough to ionize the medium through MPI and tunneling ionization and will generate plasma[34] that will defocus the trailing part of the pulse widening the beam. There are many cycles of focusing and defocusing taking place leading to filament formation (Figure 17). The length of the filament is different in different media while the free electron generation mechanisms inside the filament core are different between gases and condensed matter materials. The formation of filaments can be described as a self-action process where the laser beam undergoes spatial and temporal reshaping[36].

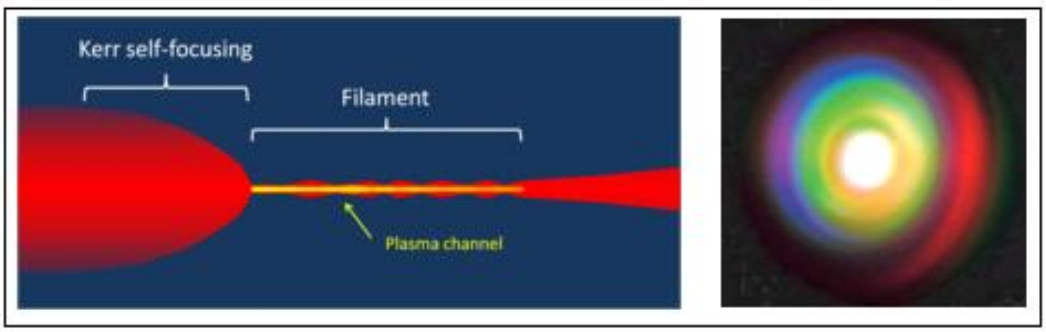

Figure 17: a) Illustration of filamentation in air b) white light [34]

3. Terahertz Time-Domain Spectroscopy (THz-TDS)

3.1 THz emission through two-color filamentation in air

Through two-color filamentation the fundamental frequency of the laser together with its second harmonic frequency are used in order to form a filament and finally to generate intense THz fields[37]. The resulting THz pulses can have energies exceeding hundreds of microjoules and extremely high electric and magnetic fields[38]. Moreover, the emitted THz pulses have extremely broad spectra, ranging from almost 0 to 60 THz, or even 200 THz that entirely cover the "THz gap", whereas in THz emission with photoconductive antennas, the emitted spectrum does not exceed 4 THz due to the electron relaxation time of the semiconductor substrate.

There are two models used to explain the nonlinear optical processes responsible for the THz emission in air. The first is the four-wave mixing (FWM) and the other is the asymmetric transient current model. The FWM is a non-linear process of third order $\chi^{(3)}$ and the emitted THz electric field can be expressed as[39]

$$\boldsymbol{E_{THz}(t) \propto \chi^{(3)} E_{2\omega}(t) E^{*}_{\omega}(t) E^{*}_{\omega}(t) cos(\varphi)} \quad \textbf{(20)}$$

When describing the THz field as a function of optical beam, eq. (20) can also be written as

$$\boldsymbol{E_{THz} \propto \chi^{(3)} \sqrt{I_{2\omega}} I_{\omega} \cos(\varphi)} \quad \textbf{(21)}$$

On the other hand, according to the photocurrent model intense THz pulses are emitted through a two-color filament as the result of a net transverse current which is formed in the plasma channel. For an appropriate phase between the ω and 2ω, an asymmetric synthesized laser electric field is formed and strips off the free electrons towards the same direction. For this model the synthesized laser field is:

$$\boldsymbol{E_L(t) = E_{\omega} cost + E_{2\omega} cos(2\omega t + \theta)} \quad \textbf{(22)}$$

After ionization, the external laser electric field accelerates the free electrons at a velocity of:

$$\boldsymbol{u(t) = -\frac{e}{m_e} \int_{t'}^{t} E_L(t) dt} \quad \textbf{(23)}$$

Assuming that the electrons velocity is zero, then the drift velocity is given by the following equation:

$$\boldsymbol{u_d(t') = \frac{eE_{\omega} sin(\omega t')}{m_e \omega} + \frac{eE_{2\omega} sin(2\omega t' + \theta)}{2m_e \omega}} \quad \textbf{(24)}$$

As a result, for θ=π/2 the symmetry is broken and a net current is formed which is given by the equation:

$$\boldsymbol{J(t) = \int_{t_0}^{t} e v_e(t, t') N_e(t) dt'} \quad \textbf{(25)}$$

where N_e is the electron density calculated from the ionization rate equation. The THz electric field is derived from the electron current density[40]:

$$\boldsymbol{E_{THz} \propto \frac{dJ(t)}{dt} = e\frac{dN_e(t)}{dt}u_d(t)} \quad \textbf{(26)}$$

A typical experimental set up for generation by two color filamentantion is presented in Figure 18 [37].

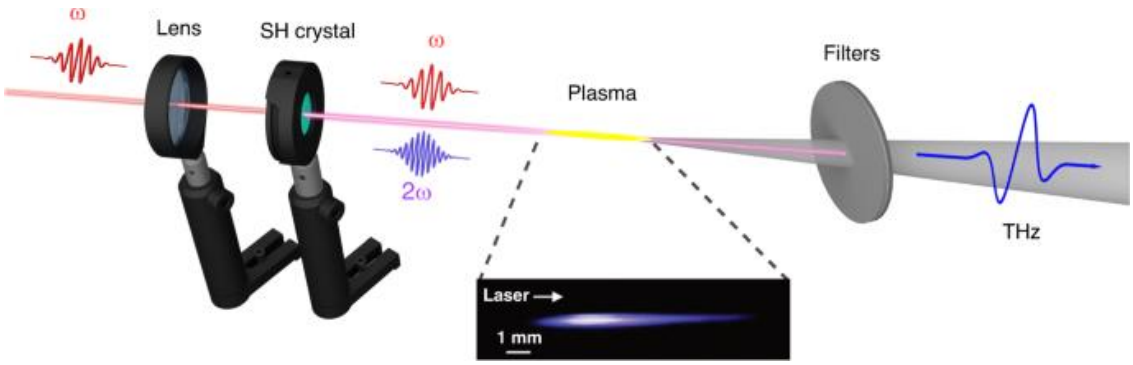

Figure 18: Typical set up for generation by two color filamentation[37]

3.2 THz detection through electro-optic sampling

Electro-optic (EO) sampling is an optoelectronic technique of optical sampling in which the propagation of THz waves through optically active crystals leads to linear electro-optic effect or Pockels effect. The Pockel's effect is closely related to optical rectification. As optical rectification is a χ^2- process for generation of THz radiation the Pockel's effect is a χ^2- process that can be used for the detection of THz pulses. Nonlinear crystals with zincblende structures such as ZnTe and GaP, are widely used for the EO-sampling method[41]. In EO, the THz field is measured by modulating a probe laser beam inside the EO crystal, where it changes the polarization ellipsoid of the refractive index of the EO crystal. The linearly polarized probe beam co-propagates inside the crystal with the THz beam, and its phase is modulated by the refractive index change induced by the electric field of the THz pulse[42-43]. The existence of the THz field changes the birefringence of the EO crystal, i.e causing the refractive index to be different for polarizations along different axes of the crystal. The electric field induced birefringence changes the polarization of the probe beam. This polarization change is converted to intensity change by an analyzer such as a Wollaston prism. Usually, a pair of balanced photodiodes is used to suppress the common laser noise while the signal is doubled.

For a zincblende crystal, such as ZnTe, when an electric field is applied, its ellipsoid of the refractive index is

$$\frac{x^2+y^2+z^2}{n_o^2} + 2_{\gamma 41}E_x yz + 2_{\gamma 41}E_y xz + 2_{\gamma 41}E_z xy = 1 \quad (27)$$

Where n_0 is the refractive index of the crystal without electric field, x,y,z are coordinate units of the ellipsoid, E_x ,E_y ,E_z are the applied electric fields along the corresponding axes and γ_{41} is the EO coefficient of the crystal. A phase delay Γ can be calculated according to the change of the refractive index

$$\Gamma = \frac{2\pi d}{\lambda}\Delta n \quad (28)$$

where d is the thickness of the EO crystal and Δn is difference between long and short axes of the ellipsoid. In order to measure this phase delay, we can use a balanced detection. Figure 19 shows the concept of balanced measurement. A linearly polarized probe beam is transformed to elliptical polarization through the electro-optic process[29]. A quarter wave plate is used to bias the polarization of the probe beam. An analyzer (Wollaston prism) is used to split the biased probe beam into s and p polarization components and a pair of balanced photodetectors measures the difference between them. When no THz field is applied, s and p polarization components will have the same intensity after the analyzer and the balanced detector gives no signal (figure 20). The presence of THz field changes the polarization of the probe beam, generating a measurable signal in the balanced detector which is:

$$S \propto sin\Gamma \quad (29)$$

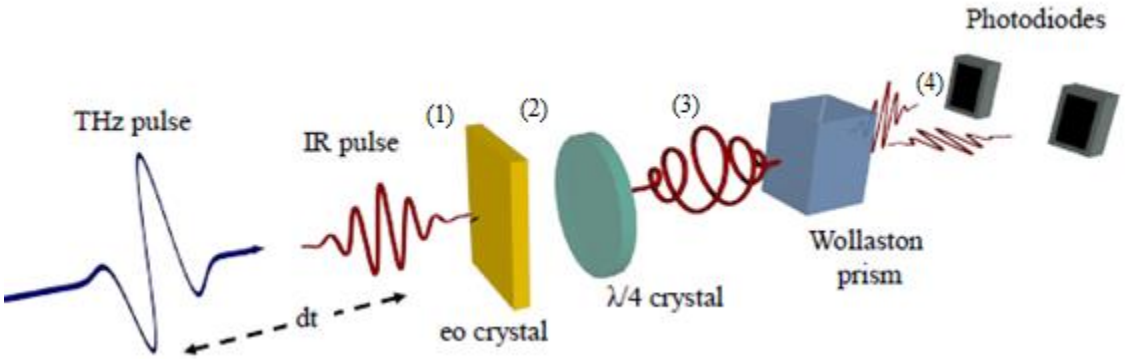

Figure 19: THz detection through EO sampling[29]

Position	(1)	(2)	(3)	(4)
No THz				
THz present				

Figure 20: How polarization is affected with THz or not in different positions during the EO sampling

3.3 THz experimental set up

A) High power sources

THz time-domain spectroscopy is a pump-probe technique in which the properties of the sample are probed with short pulses of THz radiation. After a time-delay, the probe is used to detect coherently the reflection or transmission of the pump beam. The approaches for the emission and detection of THz radiation have been already analyzed in the previous sections.

The homemade THz-TDS system used in this work operates in reflection mode and is illustrated in figure 21. A powerful amplified kHz Ti: Sa laser system delivering 35 fs pulses at 800 nm central wavelength and energy of 2.3 mJ per pulse is used. First, the ultrafast laser pulse splits into pump and probe beams by a dielectric beam splitter (90:10). The 90% is used for the generation of THz pulses and 10% for the THz detection. In our system the THz pulses are generated from a two-color filamentation. Thus, the pump beam is focused in ambient air after partial frequency doubling in a beta-Barium- Borate (BBO) crystal to produce a two-color filament and then the THz radiation. A silicon wafer is placed to stop the visible light and allow only the THz pulses to pass. Two off- axis parabolic mirrors with gold coating are used to collect, collimate and focus the THz pulses on the sample. Another pair of parabolic mirrors is used to collect the reflected THz pulses guide them into the detection crystal. The sample is mounted on a metallic surface on an X-Y-Z stage in an incident angle that can be varied between 16^{o} and 70^{o}. Moreover, the probe pulse (detection pulse) is used to probe the THz field using electro-optic sampling. It passes through an optical delay line with femtosecond resolution. Both detection and THz pulses meet on the pellicle beam splitter and then co-propagate collinearly. A balanced detector is used to measure the induced phase delay on the probe beam. Another part of the initial beam is used to excite the sample in an IR-pump/THz probe configuration. The angle of incidence of the THz beam on the sample is equal to 30^{o}, while the pump beam illuminates it at normal incidence. Finally, the whole set up is enclosed in a purged gas chamber for eliminating THz absorption from water vapor.

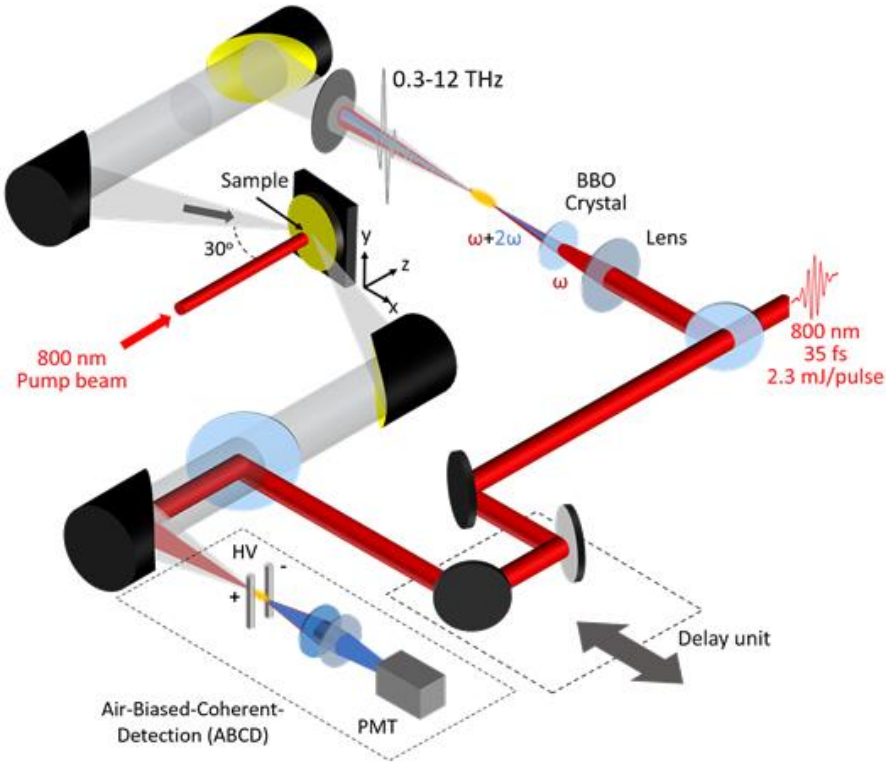

Figure 21: Schematic representation of experimental set-up

B) *Low power sources*

TOPTICA

The TeraFlash pro by TOPTICA Photonics is a compact table-top time-domain terahertz system. With the use of a fiber laser and InGaAs/ InAlAs photoconductive switches, the terahertz generation and detection can be achieved. It includes a 1.5 μm fiber laser, a fiber splitter, delay stages, driven electronics, power supply and a microcomputer[44]. The enclosed fiber coupled laser generates a beam splitting into two parts after passing through the beam splitter. There is a photoconductive InGaAs switch which acts as the terahertz detector or the emitter, where each fiber is sent to. Rapid changes in the properties of the material are the key for the terahertz detection and generation through photoconductive switches[45]. A PCA is made up of two metallic electrodes having a DC bias, deposited over a semiconductor substrate. The femtosecond laser hits the gap between the electrodes, excites electron-hole pairs in the semiconductor. The DC bias creates a potential gradient for the generated charge carriers. The charge carriers get accelerated due to this gradient thus creating an opposing field in the semiconductor. The excited charge carriers quickly recombine with the substrate thus returning the system back to its equilibrium state[46]. The polarization induced by the opposing fields creates a transient current which leads to the generation of terahertz radiation. The same manner for the terahertz detection, with the photoconductive switches detect the terahertz beam by generating charge carriers which accelerated by the electric

field of the incoming terahertz pulse. Non-linear or out of the equilibrium phenomena is observed due to the low fields.

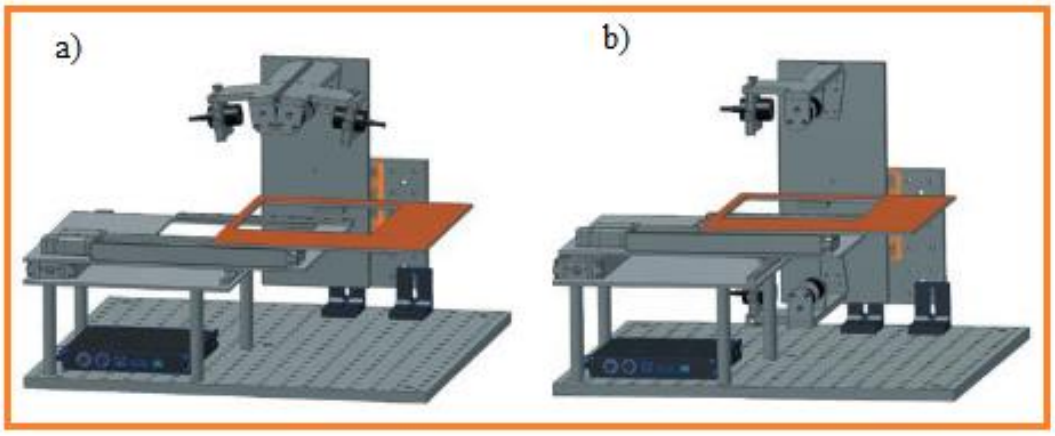

Figure 22: Schematic representation of TOPTICA experimental set-up in a) reflection and b) transmission [44]

3.4 Data Analysis

In a pulsed THz system, the waveform of THz pulse E(t) represents the temporal evolution of the pulse electric field. Through a Fourier transforming of the temporal waveform E(t) we gain access to the frequency domain and information about amplitude and phase can be extracted:

$$\boldsymbol{E(\omega) = A(\omega)e^{-i\Phi(\omega)} = \int E(t)e^{-i\omega t}dt} \quad \textbf{(30)}$$

The temporal evolution of the electric field of THz pulse is shown in Figure 23a and Figure 23c as a function of the time delay of the probe pulse, using two of the most common electro-optic crystals, a 500 m thick ZnTe and a 100 m GaP crystal respectively. After Fourier transform, the corresponding amplitude spectrum is obtained and is presented in Figure23b and Figure 23d. The main factors that limit the THz detection bandwidth in electro-optic sampling is the pulse duration of the excitation laser pulse and phase matching conditions. A laser pulse can generate THz pulses with bandwidth twice that of the laser pulse bandwidth. Also, for laser pulse duration of 35 fs, the bandwidth is estimated to be above 60 THz. The limiting factor continues to be proper phase matching. Since the frequency extent of the THz pulses is so broad, it is practically impossible to select an e.o material that fulfills phase matching requirements for all frequency components. For this reason, using ZnTe crystal we can detect within a frequency range reaching up to 3 THz while with a GaP crystal the spectral bandwidth is expanding up to 8 THz.

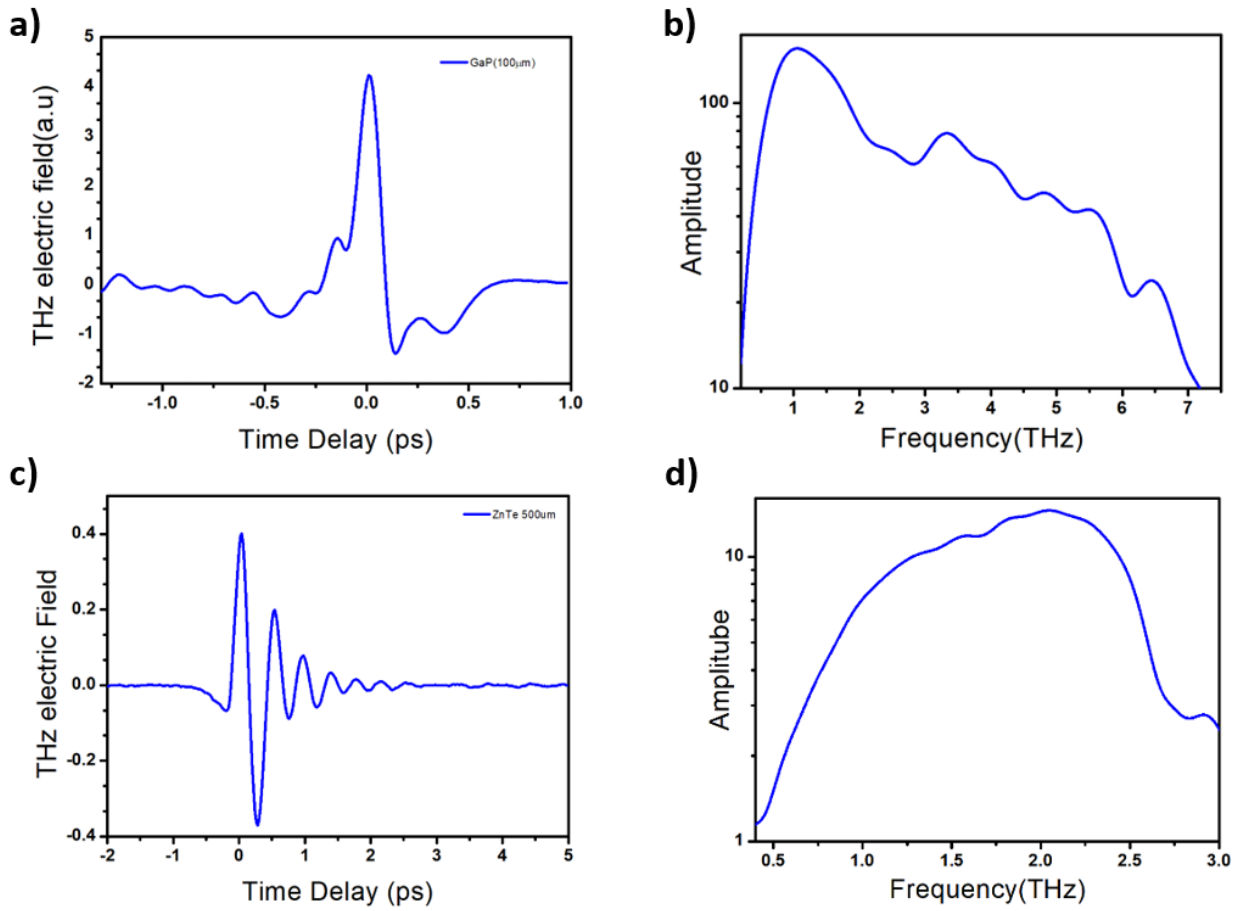

Figure 23: (a) Measured THz field with 100μm GaP crystal, (b) THz pulse spectral amplitude (c)THz electric field with ZnTe 500μm, (d) THz pulse spectral amplitude of ZnTe

The spectral resolution of THz-TDS measurement, δω, is determined by the temporal scanning range T. The frequency range of the spectrometer is limited by the response of THz source and detector, while mathematically the spectrum is significant with a bandwidth ΔΩ, which is related to the temporal sampling interval δt. In general, the bandwidth and spectral resolution of a THz-TDS are given by:

$$\delta\omega = \frac{2\pi}{T} \quad (31) \qquad ,\Delta\Omega = \frac{2\pi}{\delta t} \quad (32)$$

In a THz time-domain spectroscopic system (THz-TDS), the THz beam interacts with the sample and undergoes changes depending on the optical, chemical and structural properties of the sample are under investigation. In general, there are three main physical effects to be taken into account in the measurement process: absorption, transmission and scattering. Absorption is the energy transfer from the THz wave to certain modes of sample. The intensity I of a light beam propagating through a material obeys the Beer- Lambert law:

$$I = I_o \cdot e^{-\alpha d} \quad (33)$$

where I_o is the intensity of the beam prior to propagation through a material of thickness d and absorption α.

The optical characterization of a material in the THz regime is accomplished by measuring the electric field $E_{sam(t)}$ of the transmitted THz pulse through the sample and normalizing it to a reference electric field $E_{ref(t)}$ without any sample. (See figure 24)

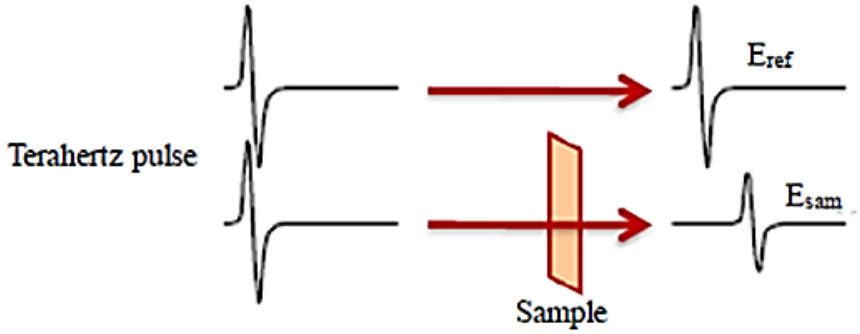

Figure 24: Representation of measuring the reference electric field and the sample electric field in the transmission mode

Taking the Fourier transform of the reference and sample electric field we can get the sample spectrum $\boldsymbol{A_S(\omega)e^{-i\varphi_S(\omega)}}$ and reference spectrum $\boldsymbol{A_R(\omega)e^{-i\varphi_R(\omega)}}$. The spectral properties of sample of known thickness d can be extracted by comparing the signal spectrum with the reference spectrum.

The absorption coefficient can be expressed as:

$$\boldsymbol{a = \left(\frac{2}{d}\right) ln\left[\frac{4n}{(n+1)^2}\frac{1}{A}\right]} \quad \textbf{(34)}$$

where d is the sample thickness and $A = A_S/A_R$.

The absorbance A(ω) is derived by the following equation:

$$\boldsymbol{A(\omega) = -ln\left(\frac{A_S(\omega)}{A_R(\omega)}\right)} \quad \textbf{(35)}$$

where A is the amplitude ratio between the sample and reference spectra.

The refractive index n is given by the following equation:

$$\boldsymbol{n = 1 + \frac{[\Phi_S(\omega) - \Phi_R(\omega)]c}{d\omega}} \quad \textbf{(36)}$$

where $\Phi_S(\omega) - \Phi_R(\omega)$ is the relative phase difference, c is the speed of light in vacuum, d is the sample thickness and ω is the radiation frequency

4. An overview of Graphene

Graphene is a 2D crystal of carbon atoms arranged in a hexagonal honeycomb lattice. It has a hexagonal honeycomb crystal structure with adjacent C-C atoms bond length of 1.42 Å and a constant rotation angle of 120°. Symmetrically, there are two sublattices inside the honeycomb lattice[47]. The valence and conduction band in graphene are smooth sided cones that meet at a point, called Dirac point as depicted in figure 25. Graphene has no energy band-gap and readily absorbs all photons at any wavelengths. As the high frequency dynamic conductivity is constant, the optical absorption of graphene is independent of the wavelength. This is an indication that graphene could potentially be used as a saturable absorber with wide optical response to cover all telecommunications bandwidths and also the mid-and far -infrared. Moreover, Dirac points are six points in the K -area at the edge of the Brillouin zone, divided into two non-equivalent three-point sets. The sets are the points K and K'. The electronic structure of graphene is easily derived from a tight binding model, resulting in peculiar Dirac cones at the corners of the Brillouin zone. Also, graphene is a semimetal because the bands with conical dispersion intersect at the Fermi level. The characteristic linear dispersion relation of electrons in graphene in the vicinity of the Dirac points makes them behave as relativistic quasiparticles, with zero effective mass[48]. As a result, the electronic and optical properties of graphene are completely different from those of a standard 2D electron gas with a massive parabolic dispersion relation, as e.g., Si and GaAlAs heterostructures. When graphene is exposed to a strong magnetic field, the massless character of the carrier manifests in an unconventional quantum Hall effect[47.] Graphene electrons can, moreover, propagate over large (micrometers) distances without scattering due to the chirality of an internal degree of freedom of carriers known as pseudospin. *As a result, graphene's electrons behave as a massless Dirac fermion*[45].

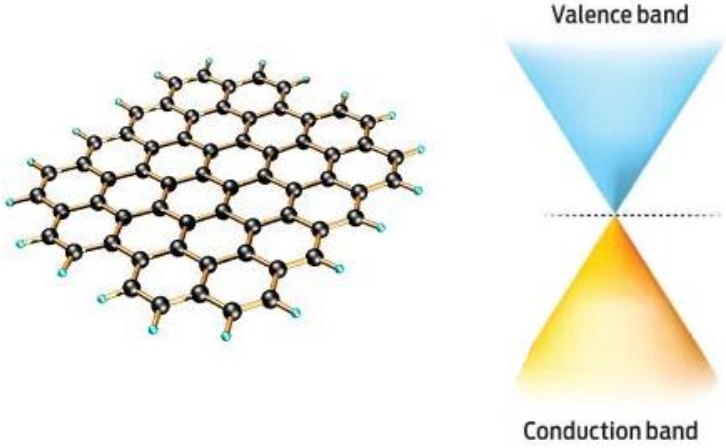

Figure 25: Band structure of graphene[47]

4.1 Optical properties of graphene

The optical properties of graphene also draw considerable attention. It has been theoretically and experimentally verified that graphene can absorb ~2.3 % of the incidence light and reflects <0.1 %. *(Figure 26)*[50]. In addition, the optical absorption of graphene layers is linearly proportional to the number of layers. The absorption of monolayer graphene exhibits a flat behavior over a long range, presenting a peak in UV region (~250 nm). Recently, it has been predicted that graphene's linear dispersion properties should lead to strongly nonlinear optical (NLO) behavior at microwave and terahertz frequencies. At higher optical frequencies, one can also expect enhanced optical nonlinearity because of graphene band structure, because interband optical transitions occur at all photon energies[48.] For pristine graphene, strong saturable absorption (SA) and four -wave mixing (FWM) has been found because of the large absorption and Pauli blocking.

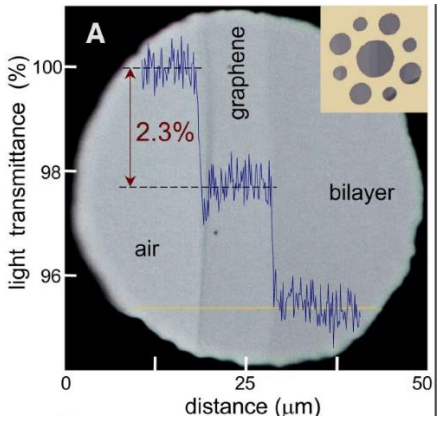

Figure 26: Photograph of a 50-mm aperture partially covered by graphene and its bilayer[47]

4.2 Electrical properties of graphene

Electrical conductivity is simply about "ferrying" electricity from one place to a different in a very relatively crude fashion; far more interesting is manipulating the flow of electrons that carry electricity, which is what electronics is all about. The electronic properties of graphene also are highly unusual. Firstly, the electrons are faster and far more mobile, which unveil the likelihood of computer chips that employment more quickly (and with less power) than those we use today[48]. Secondly, the electrons move through graphene a small amount like photons (wave-like particles of light), at speeds close enough to the speed of sunshine (about 1 million meters per second, in fact) that they behave in line with both the theories of relativity and quantum physics, where simple certainties are replaced by puzzling probabilities. which means simple bits of carbon (graphene, in other words) may be accustomed test aspects of these theories on the table top, rather than by using blisteringly expensive particle accelerators or vast, powerful space telescopes[50].

4.3 Graphene -as a highly non-linear medium

Researchers have shown that due to the unique properties of graphene were observed strong optical non-linearities in the THz range[51], which are useful for high-speed modulators[52]. In general, non-linearity of graphene is related to the transport of free electrons in the applied electric field of an incident wave while THz nonlinearities in graphene can come from both interband and intraband THz transitions[51]. Wavelength plays a vital role in exploring inter and intraband carrier dynamics in graphene. Due to Pauli-blocking effect, the interband transitions can occur, as long as, the exciting photon energy exceeds twice the Fermi-level energy[53]. These transitions are similar to photoexcitation of semiconductors, leading to creation of electron-hole pair. Also, the optical and infrared frequencies induce interband transitions whereas in THz frequencies intraband transitions appear. Simple considerations show that the interband part in THz range is negligible comparing to the intraband part. Such transitions, based on interaction of the incident light with electrons around the Fermi surface of graphene, that is free carrier absorption[54].

Several non-linear processes such as saturable absorption, high- harmonic generation, carrier heating, frequency multiplication and impact ionization in graphene have been recently reported. To begin with, the main mechanism for various applications such as optical modulators and photodetectors is *saturable absorption*[53]. For graphene, it has already been demonstrated a broadband saturable absorber. Studies have shown that the doping level, the wavelength of the laser, the number of layers and the fabrication method of graphene are some parameters which influence the value of the saturation intensity. Saturable absorption induces nonlinearity at optical frequencies and also has an effect on a decrease of the intraband conductivity of graphene[55]. At THz frequencies, interband response is decided by the carrier density, as we have already mentioned that a transition undergoes when carriers excited at twice Fermi-energy. Moreover, electron-hole pairs are created in graphene by an absorption of an optical pulse, which thermalize all charge carriers within ≈ 100 fs, concluding a transient electron distribution with an elevated temperature that *is carrier heating*[54].

Another non-linear process in graphene is *harmonic generation* under a strong THz field[56]. In 2008 Mikhailov and Ziegler, analyzed the intraband contribution via the quasi – classical kinetic Boltzmann theory, proved odd harmonics generation in graphene due to a sinusoidal excitation that can produce a square-wave-like current. Also, in 2012 Ishikawa, used a time domain approach in order to analyze the THz harmonic generation[57]. In the above studies, two conditions were demonstrated where nonlinear harmonic generation can occur. First, they predicted that the threshold electric field to observe harmonics generation in graphene is from 1 to 10 $kV \cdot cm^{-1}$, something which is easily achievable in devices[58]. Secondly, the introduction of free background electron population in graphene is the key to observe highly THz harmonic generation. These Dirac electrons can be brought in by substrate or doping or electrostatic gating which can modulate the energy transfer between THz field and graphene through nonlinear intraband conductivity mechanism. In 2018 Hafez et al, reported the generation of terahertz harmonics up to the seventh order in a single -layer of graphene at room temperature and under ambient conditions., generated

via hot Dirac fermions[59]. So, the unique electronic properties of graphene lead to strong optical non-linear processes in the THz regime, important for fabrication of high-speed devices.

4.4 Optical transitions of Graphene

Graphene has different optical properties from those of semiconductors and metals because it has a linear band structure without a bandgap[60]. In the far-infrared and terahertz spectral bands, optical conductivity is widely used to describe these features. Graphene's optical conductivity of graphene is also a strong function of temperature and Fermi level. In graphene, there are two different types of optical absorption processes[51].When light is incident on a sheet of graphene, there is a probability that an electron absorbs a photon and makes a transition to a state of higher energy. For an intraband absorption process, the initial and final states of the electron before and after it absorbs a photon are in the same band; for an interband absorption process, the two states are in different bands[61].

The two processes: intraband absorption, in which carriers from the conduction (or valence) band are excited or heated by incoming radiation, and interband absorption, in which electrons in the valence band are promoted to the conduction band through photon absorption, can be used to explain the optical properties of graphene, particularly in the THz regime[62]. Intraband absorption (also known as Drude absorption or free carrier absorption) only occurs when the graphene is electrostatically doped. On the other hand, interband absorption only occurs if there are both occupied states in the valence band and unoccupied vacant states in the conduction band with the same momentum k. If the destination of conduction band states are filled, because of the electrostatic gating, interband transition is forbidden by the Pauli exclusion principle. For frequencies $\hbar\omega < 2|E_F|$, where E_F is the Fermi energy, Pauli blocking occurs in graphene, and intraband transitions are the main optical process for this range of frequencies[61,63-64]. Graphene has a linear response in low THz fields, where its optical conductivity behaves in a Drude-like behavior. The optical conductivity at these frequencies is highly dependent on the Fermi level of graphene.

The conductivity of graphene is given by the Kubo formula and can be written as a sum of two terms, σ^{intra}, describing the intraband response, and σ^{inter}, describing the interband transitions with[65]

$$\sigma^{intra}(\omega) = \frac{2e^2 k_B T}{\pi\hbar^2}\frac{i}{\omega + i\tau^{-1}} ln\left[2cosh\left(\frac{E_F}{2k_B T}\right)\right] \quad (37)$$

$$\sigma^{inter} = \frac{e^2}{4\hbar}\left[H\left(\frac{\omega}{2}\right) + \frac{4i\omega}{\pi}\int_0^\infty d\varepsilon \frac{H(\varepsilon) - H\left(\frac{\omega}{2}\right)}{\omega^2 - 4\varepsilon^2}\right] \quad (38)$$

where the function H reads

$$H(\omega) = \frac{\sin h\left(\frac{\hbar\omega}{k_B T}\right)}{\cosh\left(E_F/k_B T\right) + \cosh\left((\hbar\omega/k_B T\right)} \quad (39)$$

ω is the angular frequency, ħ the Plank constant, k_B the Boltzmann constant, e the electron charge, τ the electron relaxation time and T the temperature.

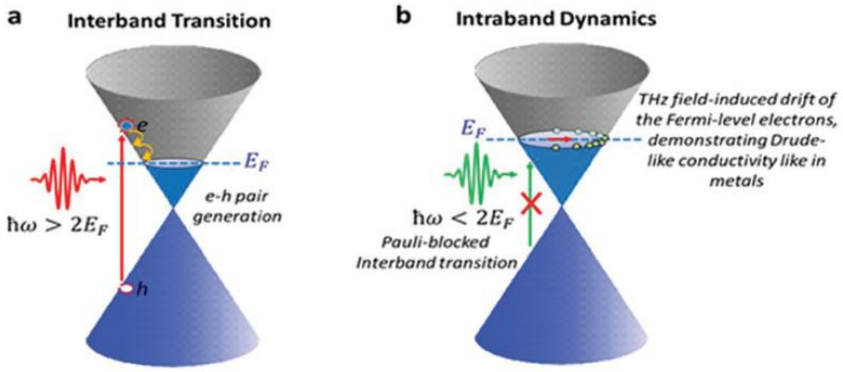

Figure 27: (a)Interband and (b) intraband absorption mechanisms in graphene[66]

5. Modulators

5.1 THz modulators

High performance THz modulators are desired in many fields such as THz imaging and THz communication. For this, terahertz modulator is growing into one of the basic devices in THz wireless communication systems, particularly within the landscape of the fast-emerging 5G and 6G technologies[67-68]. A key for high-speed communication using THz wave is quick and efficient amplitude and/or phase modulator which is used to encrypt information in the carrier wave. In addition, THz modulators based on different materials and structures in order to achieve large modulation depth, wide modulation bandwidth and fast modulation speed[69]. Based on the physical quantity they control, modulators can be categorized as for example amplitude, phase, pulse length and shape, spectrum or by the method or system of materials used to modify the wave.

In the past, all optical modulation of electromagnetic waves has been achieved using semiconductors. Typically, a laser pulse illuminates the semiconductor generating free carriers for time a period associated with the recombination time (τ). The plasma frequency is above 1THz. At that point, the surface looks "metallic" acting like a reflective surface for time scales up to $t=\tau$. THz wave is incident on this high reflectivity area which is thus modulated. This technique has been used to create THz modulators[70, 71]. The modulation behavior propagated through materials because of the changes of materials complex refractive index or dielectric constant that affected by the carrier concentration. As well as, carrier concentration can be altered by diverse fields, THz modulators can be categorized as electrically, optically and thermally driven modulators and so on. Electrical and optical modulations are the most commonly used for amplitude and phase modulation. With the use of THz modulators, we can achieve large modulation depth, fast modulation speed and wide modulation bandwidth.

Electrically driven THz modulators:

The modification of an electrical driven THz modulator is based on directly changing the device geometry electro-mechanically or by modifying some materials properties such as surface optical conductivity[72]. In these modulators, the transmittance of the incident THz radiation can be tuned by electronically tuning the conductivity of the frequency selective surface. Moreover, efficient modulation can be achieved using meta-material structures in this kind of THz modulators, where the modification of conductivity and subsequent absorption of free carriers in a small semiconductor active region located between a periodic metallic pattern. An example is a frequency selective surface structure with a remarkable control of the terahertz transmission with 80% modulation depth at frequencies near to the structure specific resonance[73].

Optically driven THz modulators:

In this kind of modulators, an external laser source is required in order to induce modulation. The repetition rate of the laser is a few kHz for the pulse energies required for giving a satisfactory depth of modulation. So, the repetition rate in many of these devices restricts the modulation speed rather than the inherent device speeds. Because of this, using this form of modulators to create small compact systems is challenging. The two different types of optically

driven modulators are based on photonic crystals and metamaterials, respectively. They have same working mechanism with electrically driven modulators. The optical Kerr effect is utilized in photonic crystal-based modulators to alter the refractive index of waveguide, which alters absorption and THz transmittance.

Thermally driven THz modulators:

Thermally driven modulators have the inherent drawback of being able to operate only at cryogenic temperatures although they can produce decent modulation. This limits the way it can be integrated in compact systems. There is a variety of demonstrations of thermally THz modulators based on semiconductors or metal oxides[74] special insulator materials with metallic phase transition[75], or superconductors, considering its THz characteristics can significantly vary with cooling[76] .Even normal semiconductor materials can be employed as terahertz modulators because carrier density, and therefore conductivity, is a strong function of temperature.

5.2 Metamaterials in THz regime

In recent years, various research efforts have been done to fill the terahertz gap, attempted by developing devices that work in THz regime such as emitters, detectors, filters, absorbers and modulators. Researchers proved that one remarkable way to manipulate electromagnetic waves is via metamaterials which promise a combination of effective permittivity and permeability values that are uncommon in natural materials[77]. Importantly, metamaterials play a vital role in terahertz regime as they break the natural material limitations. The structure of these devices is artificial such as metasurfaces. Metasurfaces are electromagnetically ultrathin artificial materials with macroscopic properties defined by the architecture of the building blocks, the meta-atoms[78]. Adjusting the meta – atoms enable to control over different aspects the electromagnetic waves and the realization of unusual electromagnetic functions. Within this framework we present various groups of the metasurface configurations incorporating different constituent materials.

5.2.1 Metamaterial Perfect Absorbers

Metamaterial Perfect Absorbers (MPA) have become one of the most promising platforms in attempts to achieve perfect absorption. They are designed to absorb all of the incident light at their design frequency. Typically, absorbers consist of two metallic layers separated by a dielectric space. The top metallic layer links with an external incident electric field to customize the electric response, while the top metallic layer and metallic ground plane or metallic wires work together to modify the magnetic response[79]. Both, electrical and magnetic response can be modified by altering absorbers shapes and geometrical parameters. Especially, in terahertz regime a perfect absorption can be obtained by thin metasurface-based absorbers, and high absorption is derived through impedance matching of the environment and dielectric loss at and around the resonant frequencies[80].

Many approaches have proved that a good candidate material for the design of a metasurface tunable THz perfect absorber is graphene. In bibliography, there are many complex

structures for how a graphene-based THz absorber can be designed. First, Su et al, demonstrated an ultra-thin terahertz metamaterial absorber based on graphene/MgF_2 multilayer stacking unit cells arrayed on an Au film plane[81]. Another structure was by Zhang et al. where a graphene-based broadband tunable absorber consisted of a periodic array of a dual electric LC metamaterial unit fabricated on a multilayer structure composed of Au/BaF_2/graphene materials from the bottom to the top[82]. Also, Liu et al, designed a broadband terahertz absorber based on singular graphene patches metasurface and metal backed dielectric layer[83]. In all researches, they designed a complex graphene-based absorbers for total absorption and modulation effect. Nevertheless, there are simple structures to design a graphene-based THz absorber which consist of a single-layer graphene placed on ionic liquid substrate, back-plated by a metallic back-reflector.

5.2.2 Principle of Absorbers

THz absorbers can be categorized as broadband and narrowband absorbers[84]. The first are based on subwavelength surface structures that minimize surface reflection from the top of lossy substrate materials, resulting in perfect absorption at frequencies higher than the lower cut off frequency of 0.7 THz[85]. On the other hand, narrowband absorbers are mostly based on frequency selective metamaterials consisting of periodic, resonating metal structures. With the combination of metamaterials on the top of the cavity and with the reflector on the back, a metamaterial absorber is capable of frequency-selective absorption in the multiband THz frequency range. Moreover, classical examples of narrowband absorbers are Dallenbach, Jaumann and Salisbury absorbers. The Dallenbach perfect absorber consist of a homogeneous lossy dielectric layer on top of a metallic ground plate. The thickness of the layer and its material properties like permittivity and permeability, have to be carefully chosen such that the reflected light is totally suppressed via impedance matching. The layer thickness of a Dallenbach is close to quarter wavelength in the dielectric, so that the input impedance is real. The loss tangent of the dielectric is chosen so that the input resistance is matched with the free-space impedance [86]. In contrast, the Salisbury perfect absorber consists of a resistive sheet on top of the metallic ground plate separated by a dielectric spacer as shown in figure 28. This absorber relies on the absorption in the resistive sheet. The refractive index of the dielectric spacer plays an important role on choosing the thickness of the layer. The basic principle of the Salisbury absorber based on destructive interference of the reflected ray and a suppression of the transmitted light [84,85]. Finally, the designs of the Salisbury and Jaumann absorber are almost similar where the Jaumann absorber employs metal-dielectric-metal layers. However, in the Jaumann absorber, the dielectric layers after the metallic ground plate are repetitively stacked with varying dielectric layer thickness. Each of these dielectric layers is particularly tuned to absorb specific wavelengths[85].

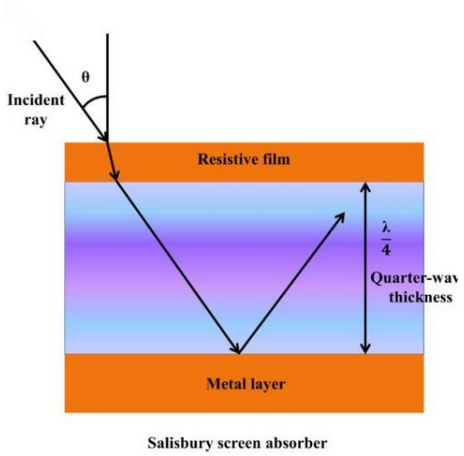

Figure 28: A representation of Salisbury screen absorber[86]

The simple structure for a perfect absorber would be a homogeneous absorbing medium in contact with air. It is a structure which has a zero-reflection and transmission coefficients for normally at one given frequency. The absorbing medium should have both absorptions, the wave impedance of unity to match the impedance of air and the imaginary part of refractive index. In the case there is an impedance mismatch, there is always a reflection which is undesirable for a perfect absorber. Also, for a perfect absorber with unity absorption A, reflection R and transmission T should be minimize. The absorption A is given by: A= 1-R-T, the transmission is easily minimized by utilizing a metallic back plate. The reflectivity of an incident electromagnetic wave normal to a metamaterial absorber is given by:

$$\boldsymbol{R} = \left|\frac{\boldsymbol{Z(\omega)}-\boldsymbol{Z_0(\omega)}}{\boldsymbol{Z(\omega)}+\boldsymbol{Z_0(\omega)}}\right|^2 \qquad \textbf{(40)}$$

where $\boldsymbol{Z(\omega)}=\sqrt{\boldsymbol{\mu(\omega)\mu_0/\varepsilon(\omega)\varepsilon_0}}$ is the impedance of the metamaterial absorber and $\boldsymbol{Z_0} = \sqrt{\boldsymbol{\mu_0/\varepsilon_0}}$ is the impedance of free space. The condition of the reflectivity to be zero is $Z(\omega)= Z_0(\omega)$. Also, the condition $\mu(\omega)=\varepsilon(\omega)$ should be satisfied. For all materials $\mu=1$ due to there are no natural magnetic materials in optical regime. Finally, by tuning the electric permittivity $\varepsilon(\omega)$and the magnetic permeability of metamaterials, allow us to reach perfect absorption at a certain frequency by impedance matching with free space[87].

Coherent Perfect Absorption (CPA)

The absorption of electromagnetic energy of a conductive material can be enhanced due to interference between the incident and reflected waves[43]. It is possible for a device to perfectly absorb an incident electromagnetic wave if all the wave components scattered by the device destructively[44]. Coherent perfect absorption (CPA) has become a popular research topic due to its potential use in nanophotonic applications like optical modulators, sensors and optical switches. In order to achieve perfect absorption, we will introduce the use of two simple structures. The first structure is a single mode resonator which can perfectly absorb the input wave when the critical

coupling condition is satisfied. The second structure consists of a thin absorbing sheet (e.g., graphene) and a dielectric spacer on top of a thick metal layer. 2D materials such as graphene, provide further tunability in the CPA response through controlling their doping level by using appropriate gating voltage configurations. The optical absorption in graphene at optical wavelengths is 2.3 % whereas in long wavelengths such as THz and microwave, the absorption can be increased at 50% when the surface impedance of graphene (Z_G) matches half of the free space impedance, $Z_G=1/\sigma(\omega) =Z_0/2$ where Z_0 is the free space impedance matching and $\sigma(\omega)$ the optical conductivity.

In order to achieve coherent perfect absorption, we need to define the correct thickness of the cavity in order to achieve destructive interference. In graphene, the electric field is maximized and extensive modulation of absorption is possible when the substrate optical thickness is an odd multiple of a quarter wavelength. In contrast, the electric field in graphene disappears and there is no absorption when the substrate optical thickness is an even multiple of a quarter wavelength. For example, the first absorption band of Fabry Perot occurs at $\lambda/4$.

The total perfect absorption can be calculated from the complex transmission and reflection as

$$\boldsymbol{A = 1 - |r|^2 - |t|^2} \quad \textbf{(41)}$$

Since the ground plane is completely opaque, it is safe to assume that t=0, and in order to obtain maximum absorption, |r| must be minimized. As we mentioned in previous sections, the metamaterials absorbers' characteristics can be tuned in order to optimize the impendance matching with air and minimize reflections

5.3 Graphene-based THz absorbers

In the quest of achieving the necessary tunability to efficiently undertake THz modulation, various materials and devices have been explored, such as diodes[88], phase matching materials[89], bulk semiconductors, two-dimensional materials and more[90]. One of the most promising such materials is graphene, whose unique mechanical and optical properties stand in the center of the research attention in recent years[91]. So far graphene has been used into a plethora of opto-electronic THz components controlling both propagating and localized surface plasmons from waveguide modulators[91], emitters and detectors for terahertz radiation[93] and metasurfaces with exotic functionalities. Additionally, graphene is expected to play a key role in space-time-modulation, which further expands the wave interaction impact [94-96].

Graphene, as a 2-dimensional semiconductor material, exhibits a Drude-like response in the THz part of spectrum, due to its easily created and controlled free carriers**.** Electrostatic or magnetic field tuning, as well as chemical doping, can be used to modify the material's optical properties[97]. Specifically, chemical doping tuning the electronic properties of graphene by controlled doping with holes or electrons. An example of this method in graphene is via HNO_3 which is a p-type dopant for carbon-based nanomaterials such as carbon nanotubes and graphite. Between carbon atoms NO_3^- molecules so that the Fermi level is shifted and the carrier

concentration increases leading to an increase in the conductivity of graphene film. As long as, with electrostatic gating is observed modification of Fermi level and charge carrier density[98]. Additionally, graphene optical response can be modified in an ultrafast manner; hot electrons driven by the excitation by optical pulses can lead to a sub-ps transient modulation of its conductivity[99]. Similar effects are observed under the intense THz pulse excitation, where hot carrier effects dominate the response. In fact, graphene is considered to be a particularly highly nonlinear material at THz frequencies[64]. The nature of this nonlinear response has been related to the collective thermodynamic response of the background Dirac electrons under the application of intense THz fields, resulting in THz-induced carrier heating. Many interesting nonlinear features of graphene have been observed, which may be further facilitated by the rapid development of high-power THz sources[100-102]. Experiments have shown that the emission of THz induced high harmonics[68], graphene plasmon nonlinear absorption[103], saturable absorption,[104] and the electric tunabilty of the graphene's nonlinearity.[105]

5.4 Ways to modulate a THz modulator

Several methods have been reported in literatures to make a graphene absorber tunable. Most known techniques are through electrical and optical modulation[106]. Electrical modulation first alters the incident THz waves amplitude by controlling the concentration of electrons in the substrate materials or structures using bias voltage. In 2016, Kakenov et al, demonstrated a new type of tunable THz cavity which enables them to observe tunable coherent perfect absorption (CPA) [107]. THz cavity formed by a large area graphene layer, a metallic reflective electrode and an electrolytic medium in between. They proved that with this device conformation can be designed flexible active THz surfaces with voltage-controlled THz reflectance and are allowed direct measurement of Fermi energy[107].

Furthermore, optically tuned THz modulators are the other route for modulating THz waves. When an optical excitation, is applied on the surface of graphene structure, large density of carriers is generated and diffused into graphene, which leads to conductivity charge of graphene and also transmission of THz signal. In 2019, Tasolamprou et al, reported an ultrafast absorption modulation in a graphene-based thin film absorber. It consisted of a uniform CVD grown graphene sheet on an SU-8 dielectric substrate that is grounded by a metallic ground plate. They observed an enhancement of absorption due to coherent interference of the impinging and reflected waves where they are in phase at the lossy graphene sheet. The modulation of THz absorption is achieved by applying an optical pump signal modifying the conductivity of graphene. This phenomenon is associated with hot carriers' generation, an increase of temperature and a dominant increase of scattering rate over the carrier concentration[108].

Taking into account the results of these experiments, along with the highly non-linear response of graphene at THz frequencies, the aim of this master thesis is to research if we could modify a THz absorber in a non-linear way using the interaction of intense terahertz waves in a graphene-based modulation device[109].

6. Experimental part: Materials, Results and Discussion

6.1 Samples

In this work, we used three different graphene-based devices which consisted by a thick porous membrane with thicknesses 25μm, 50μm and 75 μm as cavity layer, sandwiched between a chemical vapor deposition (CVD) grown single layer graphene as the top electrode and a gold electrode as a back reflector. In Figure 29, it is shown the graphene absorber device. The porous membrane was soaked with room-temperature ionic liquid electrolyte (DEME-TFSI) that allowed us to fine tune the Fermi energy of graphene with external gating between the graphene layer and the grounded gold electrode.

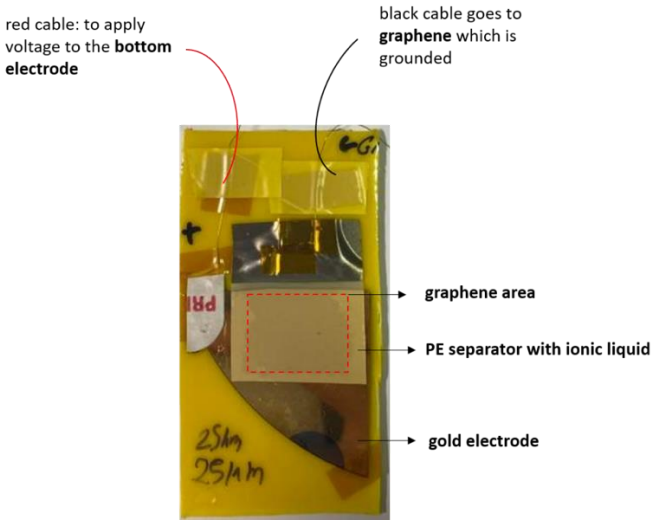

Figure 29: Graphene absorber device

6.2 Experimental Measurements

In the following figure (Figure 30), we demonstrate an electrically gate-tuned graphene-based Salisbury screen device. A basic Salisbury screen design, where a homogeneous graphene sheet is placed on top of a dielectric substrate, back-plated by a metallic back-reflector, can produce a modulator with tunable and almost unity (perfect) absorption. If there are no losses in the dielectric layer and the metallic plate reflects light almost perfectly, the only source of losses in the cavity is the graphene sheet. Only a small portion of the impinging wave is absorbed by graphene in a freestanding form (i.e., without the back-reflector). The operation principle of a modulator is a coherent interference of two propagating waves, incoming and back-metal reflected wave on the graphene sheet for perfect absorption realization.

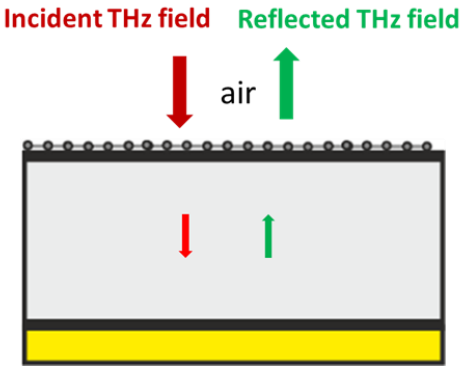

Figure 30: Schematic representation of the graphene absorber structure.

By applying voltage between the graphene layer and the grounded back gold electrode, the Fermi level of the graphene and hence the carrier density can be dynamically controlled with a corresponding change of surface conductivity of graphene. This modified optical conductivity is translated into variation of the complex permittivity of the atomically thin graphene layer, which is turn results in changes to the transmitted terahertz wave through the metamaterial. Due to the nature of the growth and transfer processes, the graphene layer is positively doped when no voltage is given to the device. Without any electrostatic gating, the doping level is enough to satisfy the coherent perfect absorption conditions.

Figure 31 shows a schematic representation of graphene-based absorber under a bias voltage that polarizes the ionic liquid in the membrane, electrostatically dopes the graphene layer and alters the conductivity. By applying bias voltage on the single layer of graphene, carriers are gathered at a specific area. Whereas, the addition of the ion gel between metal and graphene made it possible for carriers to be uniformly allocated to the whole graphene area. So, ion gel, the most effective dielectric with high capacitance is used to control the Fermi energy of graphene. Because of its good mechanical flexibility, excellent electrochemical and thermal stability, ion gel can be compatible with tunable graphene plasmonic devices on various substrates[112].

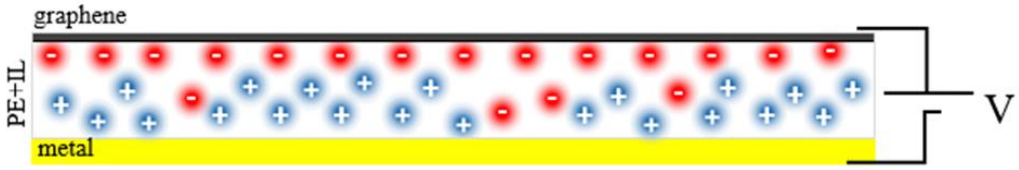

Figure 31: Carriers' formation through applying voltage in graphene cavity

6.3 Electrical Measurements

Many studies have shown an electrically tunable coherent perfect absorption (CPA) of terahertz radiation in graphene[110]. Fan et al, predicted that a highly doped monolayer graphene which Fermi level is close to 1 eV, can absorb 100% of THz radiation[111]. THz absorption can be controlled efficiently by electrical means by varying the doping level. Under the same concept it was experimentally shown that, our samples gave us the opportunity to measure directly the Fermi energy of graphene by varying the applying voltage and observing the absorption behavior. So, we demonstrated flexible active THz surfaces with voltage-controlled THz reflectance.

For the electrical measurements, we used a THz cavity consisted by single-layer of graphene placed on ionic liquid substrate, back-plated by a metallic back-reflector. During the experiments, we applied gate voltage to our samples by connecting voltmeter to the electrodes of our sample (red cable to the bottom electrode and black goes to graphene which is grounded) and used different experimental methods (low and high-power system and TOPTICA). Finally, we measured the reflectivity spectrum of graphene-based absorber under different bias voltage.

i) Using a Low Power THz source

For the linear characterization of the samples, we adopted a THz system based on photoconductive antennas from TOPTICA. The system delivers 50 fs pulses at 1560 nm central wavelength. The optical pulses are split into two parts: one used for detection and other for generation. Photoconductive antennas are used for both detection and generation. Two pairs of parabolic mirrors are used to guide the terahertz pulses from the emitter to the sample and then to the detector. The time delay between the THz and optical pulse on the detector can be adjusted by a mechanical delay stage changing the beam paths lengths. As a function of time, the electric field amplitude and phase of the THz waveform can be mapped out by scanning the delay stage. Finally, the whole setup is enclosed in a purged gas (e.g., N_2) chamber for eliminating THz absorption from water vapor.

In these experiments we aimed to electrically characterize the samples under study. In detail, we measured the reflected THz electric field of the graphene-based absorber under different gate voltages for three different thicknesses 25μm, 50 μm and 75 μm, as shown in figure 32. By comparing the THz electic fields for the different thicknesses, we come to the conclusion that there is a dependence on Fermi level and that the corresponding wave function's shape changes with thickness due to the reflections from different levels.

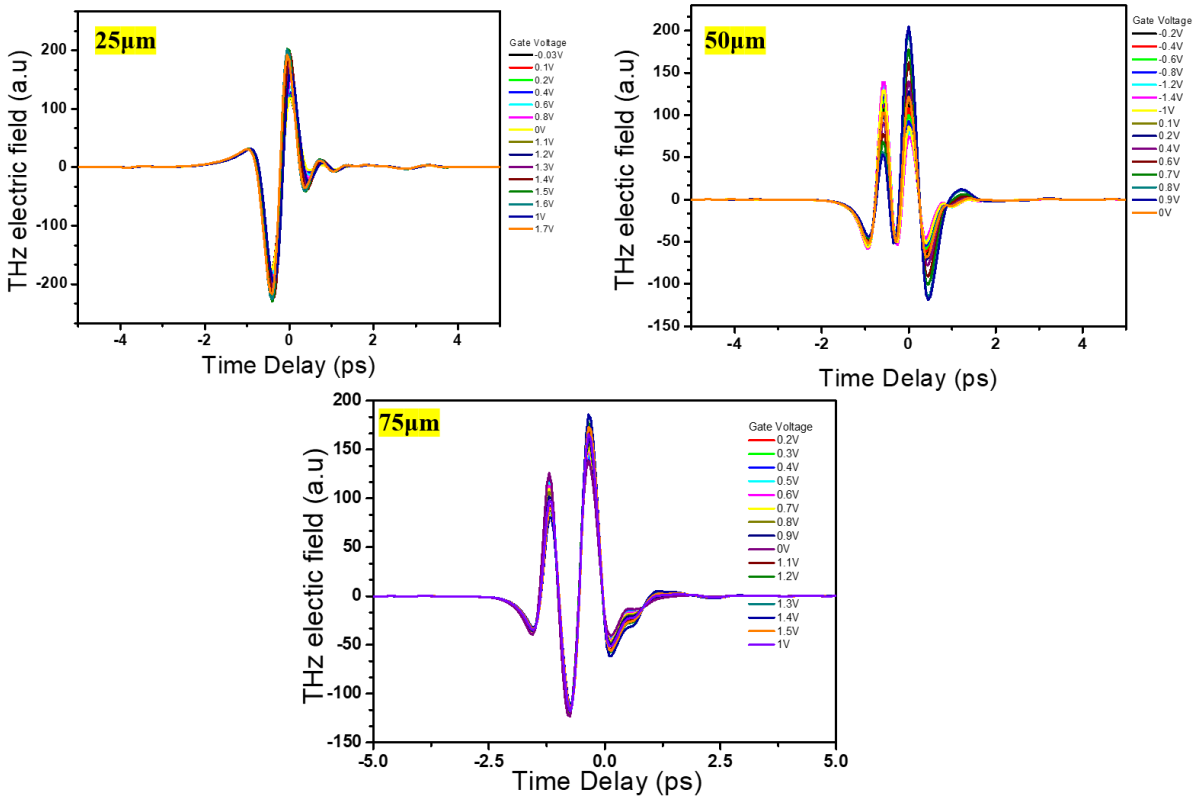

Figure 32: THz electric field of the cavity under different voltage

Then, we tried to identify the charge neutral point (CNP) by looking for the minimum reflectivity of the graphene layer by recording the first peak amplitude of the THz electric field coming from the first surface of the sample (the graphene layer). CNP is equal to the Dirac point with same number of holes and electrons at graphene. In Figure 33, we plot the THz electric field as a function of gate voltage for three different thicknesses, 25µm, 50 µm and 75 µm. First, the sample with thickness 25µm has the Dirac point at 1.5 V , the Dirac point of 50µm is 0.9 V and 1.4V is the Dirac point of 75µm. For all thicknesses the Dirac point is used as a reference for our analysis.

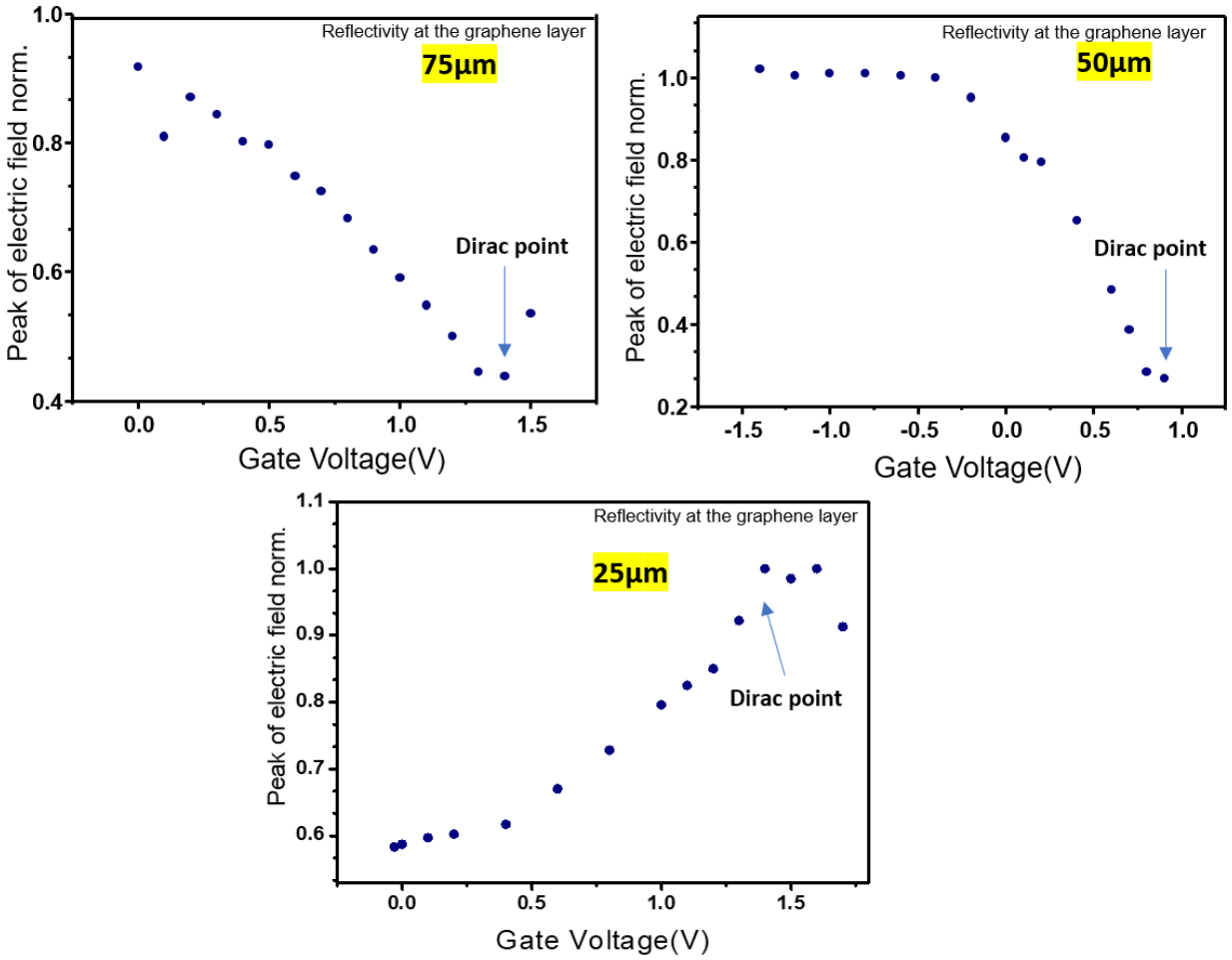

Figure 33: Reflectivity at the graphene layer under different gate voltage

Figures 34 a,b,c show the measured reflectivity spectra from the cavity under different bias voltages and thicknesses. In Fig.34 (a), the membrane thickeness is 25 µm and the incidence angle is 8^{o} and we observe a resonace at 2.4 THz. Respectively, in Fig.33 (b) with membrane thickness 50µm, we observe two resonances at 0.9 and 3.1 THz and in Fig.33 (c) with membrane thickness 75 µm we observe multiple resonance absorption peaks at 0.5, 1.8 and 3.2 THz.To maximize the absorption, we need to minimize the reflection from the top surface and achieve constructive interference of the incident and reflected wave at the graphene sheet.

In Figure 34 (c) in the range between 0.9 to 1.2 THz, we observe a reverse behavior of the resonance which hasn't been fully studied. In the literature, researchers name this behavior as antiresonances. Especially, at antiresonance the intensity inside the cavity is always smaller than the incident intensity.So, we obtain no bandwidth liminations and no absorption condition.

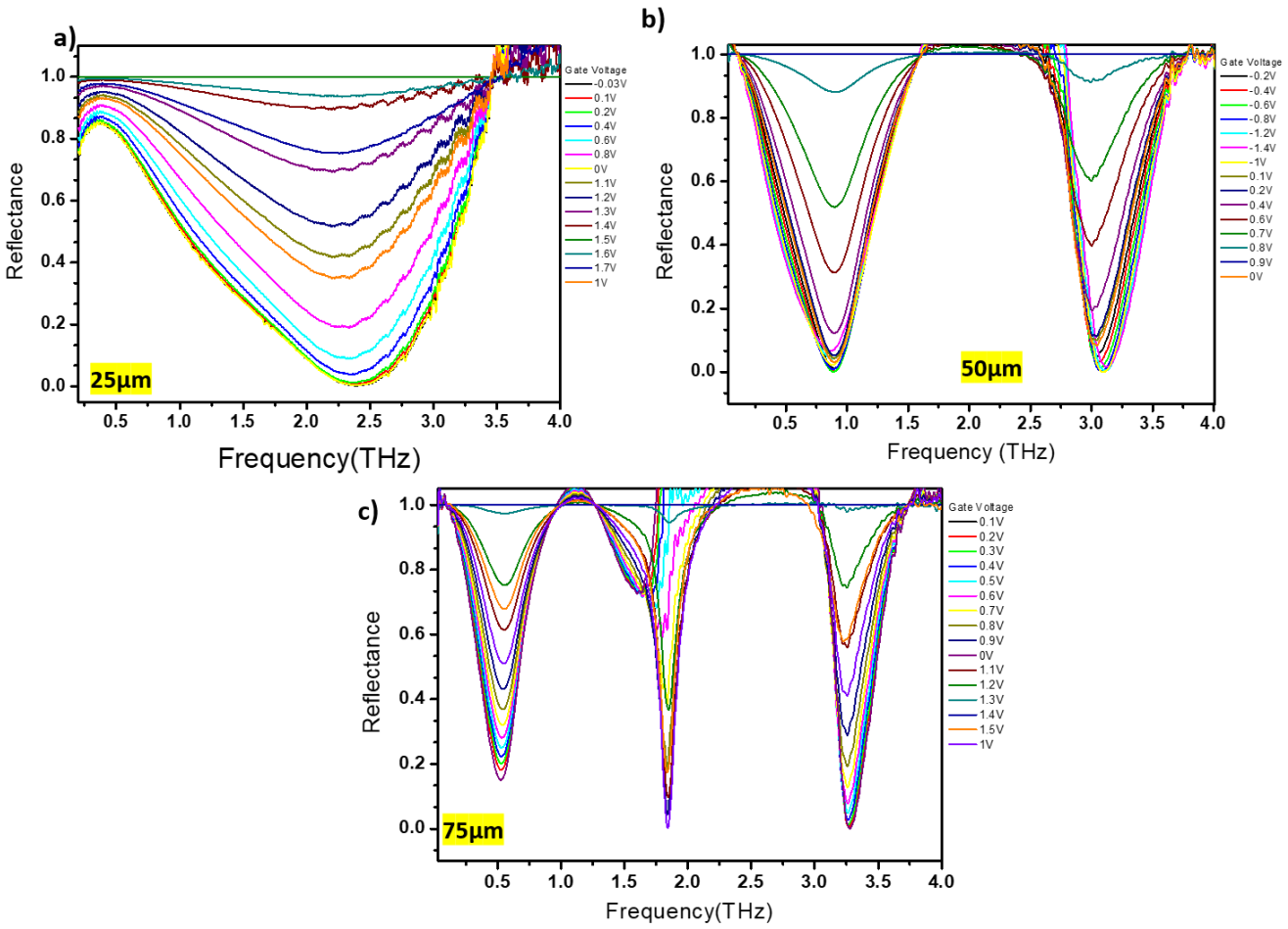

Figure 34: Reflectivity spectrum of the cavity at different bias voltage a) 25µm b)50 µm c)75 µm

ii) Using a High-power THz source

In a step further, we investigated the electrical response of the samples in a powerful THz time domain spectrometer (THz-TDS) which is based on two-color filamentation of ultrashort laser pulses in air and operates in reflection mode[109]. It uses an amplified kHz Ti: Sapphire laser system delivering 35 fs pulses at 800nm central wavelength and a maximum energy of 2.3 mJ per pulse. The most intense part of the initial beam is focused in ambient air after partial frequency doubling in a beta-barium-borate (BBO) crystal to produce a two-color filament and, subsequently, THz radiation (>200 kV/cm). The emitted THz pulses are focused at the sample and after being reflected are guided to the detection stage. Another part of the initial beam is used to excite the sample in an IR-pump/THz-probe configuration. The angle of incidence of the THz beam on the sample is equal to 45^{o}, while the pump beam illuminates at normal incidence. For the detection of the THz pulses, we have chosen electro-optic detection in a 100 µm thick gallium phosphide (GaP) <110 > crystal. The detection crystal was optically contacted to a 2 mm thick GaP <100 > crystal in order to avoid any Fabry-Perot spectral oscillations, extending the available window to 12 ps. The whole

experimental set up is enclosed in a purge gas chamber to avoid water vapor absorption of the THz radiation, and all measurements are performed at low levels of humidity.

We recorded the THz electric field of our cavity under different voltages, from -6 V to 5.5 V. We followed the same procedure as the measurements with the low power THz system in order to identify the charge neutral point (CNP) and the Dirac point which is the reference. In figure 34, we present the THz electric field after being reflected from the cavity for different voltages. We observed two different peaks because we had a very high bandwidth of the THz pulses and we clearly distinguished the two layers of the cavity. So, the first peak came from graphene layer at 0.01 ps and the second one came from metal at 1.1 ps.

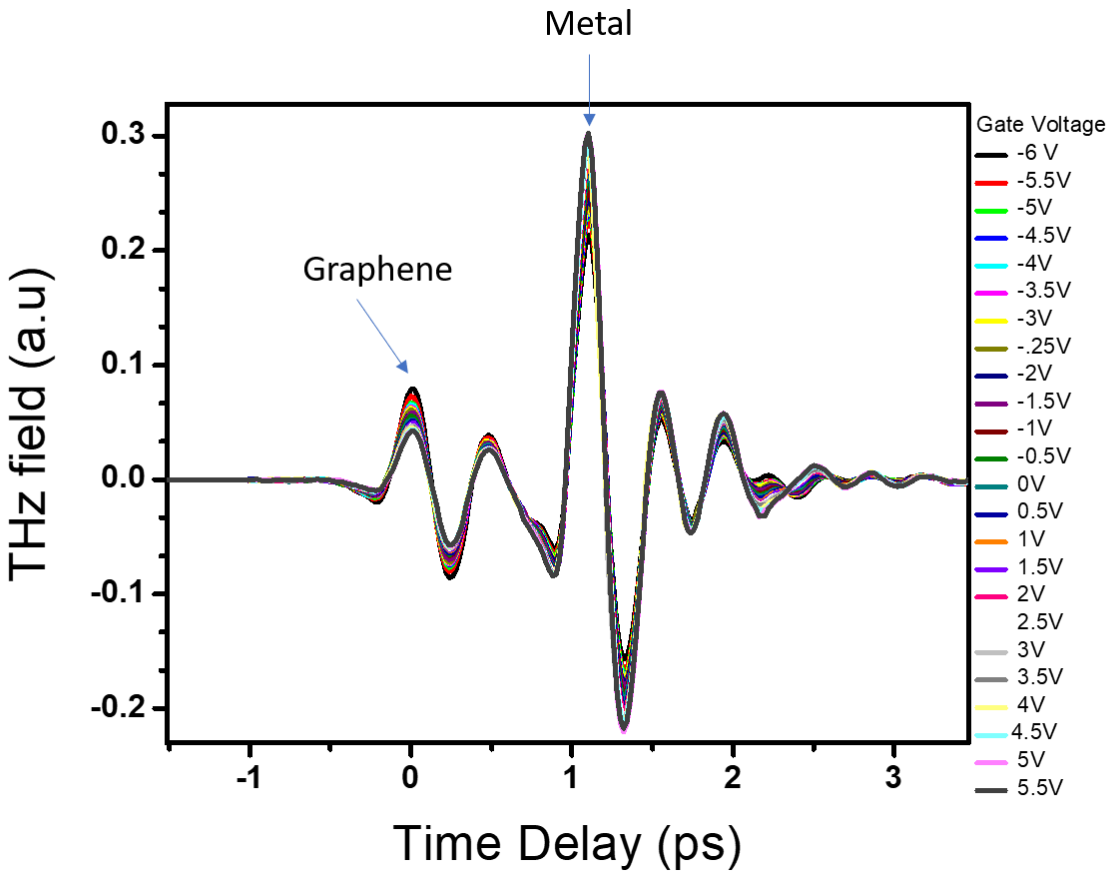

Figure 35: THz electric field of the cavity under different voltage

We concentrated on the graphene layer by recording values as a function of value of electrostatic gating, and as a result we can get the following graph depicted in figure 35. The THz reflectance of the graphene layer is sensitive to changes of the conductivity, so we used this graph in figure 36 to estimate the Dirac point which is at 5 V. So, by changing the Fermi level we can strongly affect the reflectivity of the device.

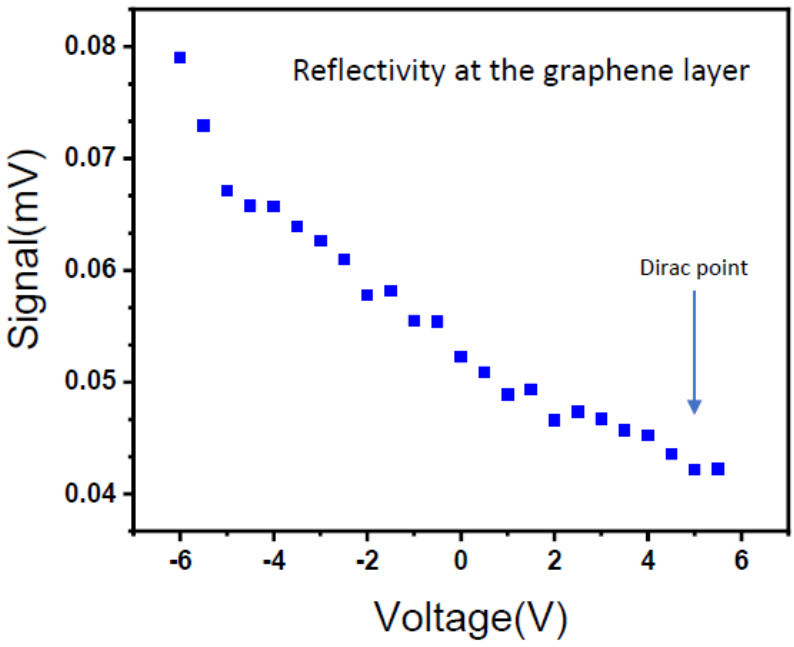

Figure 36: Reflectivity at the graphene layer under different gate voltage

Figure 37 shows the measured reflectivity spectrum of our device under different bias. We observed three resonances at 1.3, 2.3 and 3.2 THz frequencies. The biggest reflection is from the first resonance dropped down to 0.2. Perfect absorption didn't take place. Comparing the low and high THz source as depicted in figure 38, we observed that perfect absorption conditions demonstrated in the low power THz source could not be achieved under the illumination of these THz pulses indicating a THz induced disturbance of the perfect absorption conditions. Something that shows us, that it is a non-linear behavior that will be investigated with further measurements in the next section.

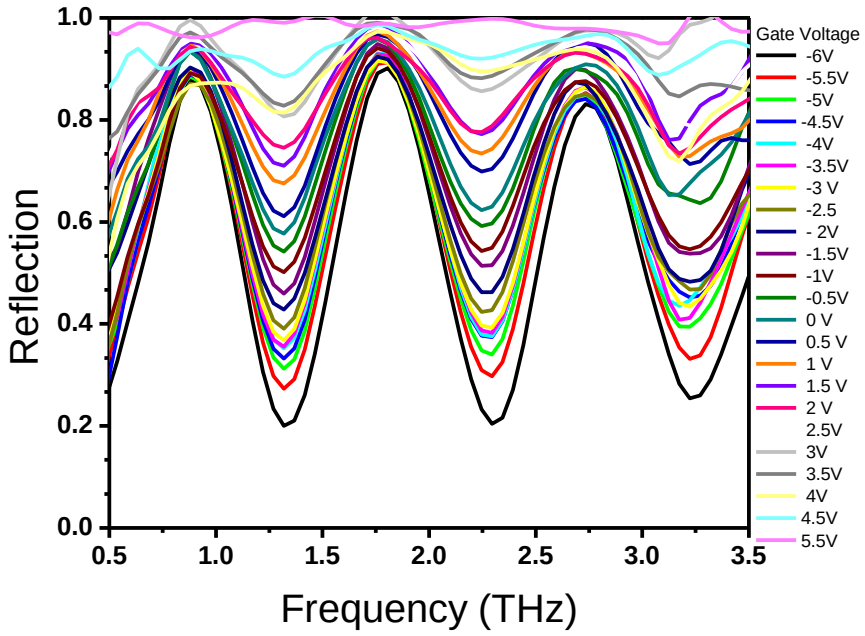

Figure 37: Reflectivity spectrum of the cavity at different bias voltage

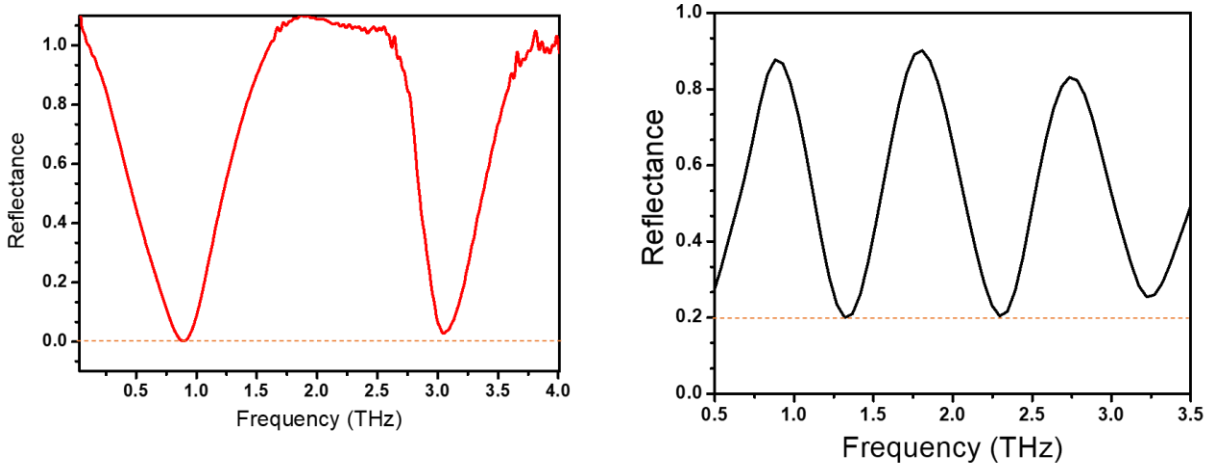

Figure 38: Compare low with high THz source

6.4 High-power THz Non-linear measurements

In order to study why we could not achieve the perfect absorption conditions under the excitation of intense THz fields, we developed a more powerful THz system. It is again based on two-color filamentation scheme, however in this setup we could focus the THz beam strongly on the sample increasing this way the incident THz field strength to values up to 700 kV/cm. The THz beam illuminates the sample at an angle of 16^{o} with a TM (transverse magnetic) polarization. During the

experiment, we controlled the strength of the THz field on the graphene sample with a pair of wire grid polarizers. The device was characterized in the range of field strengths between 102 and 654 kV/cm.

Figure 39 shows normalized measured THz electric fields for the cases of the lowest and highest available THz field strengths. Due to the high bandwidth of our THz-TDS system we are able to resolve both reflective interfaces of the device that manifest themselves as two distinct peaks on the THz field: the first one at -0.25 ps originating from the reflection of the THz pulse on the graphene layer and the second one at 0 ps originates from the back reflector as it is shown in Figure 39 (b). The outcome of figure 39 (a), shows as the THz field strength increases, we record a drop on the THz reflectivity of the graphene layer compared to the one from the gold back reflector. This indicates a THz-induced negative photoconductivity on the graphene layer. Additionally, we observe an overall modulation of the THz electric field shape indicating also a modulation of the THz field shape indicating also a modulation of the THz field phase.

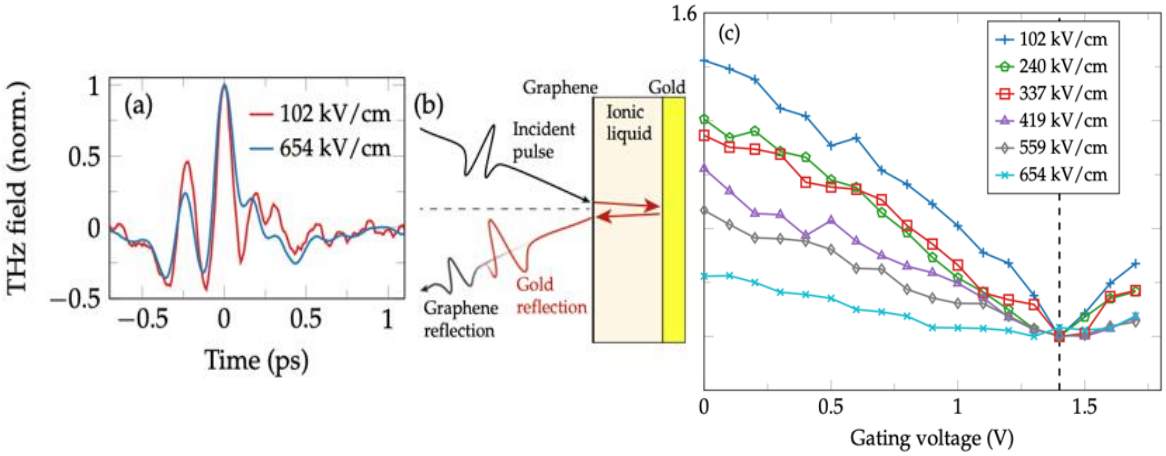

Figure 39: a) Normalized THz electric fields in the case of 102 KV/cm and 654 kV/cm, b) Schematic representation of the formation of the THz filed shape after its reflection on the graphene sample, c) THz reflectivity of the gated graphene layer alone, as a function of both THz field strength and the Fermi energy level, defined by the gating voltage. All curved are normalized to the response at the CNP of graphene indicated with dashed line at 1.4 V

The nonlinear behavior is depicted more clearly in the electrical response of the graphene layer in the presence of the external electrostatic gating. Moreover, we measured the THz reflectivity variation only of the graphene layer by recording the peak of the THz electric field that corresponds to the graphene layer (time=-0.25 ps) as a function of the gate voltage. Figure 39 (c) shows the reflectivity variation for different incident peak electric fields in the range of 102 to 654 kV/cm. All curves are normalized to the charge neutral point of graphene (dashed line at 1.4 V) defined as the gating voltage, at which the graphene resistance becomes maximum and, consequently, the THz reflectivity becomes minimum due to the increased transmission. We

observe that the graphene THz reflectivity induced by the gating voltage depends nonlinearity on the THz field strength. At low THz fields, we record a modulation of the THz reflectivity up to 50% at 0V. However, at high THz field strengths, this modulation drops to 10%.

The THz-induced photoconductivity modulation, is expected to impact the absorption and phase characteristics of the whole device. The following measurements were performed at 0V where the maximum modulation on the graphene reflectivity was observed. At Figure 40 (a) and (b) are shown the normalized reflectance at CNP and the associated phase spectra of the device for different THz field strengths. At low THz field strengths our device operates at perfect conditions, presenting a resonance at frequency f=2.33 THz defined by the device design and the angle of the incidence of the THz radiation. The reflectance of the device at this frequency drops down to $9.2 \cdot 10^{-5}$. However, as the THz field strength increases, the perfect absorption conditions are disrupted and the reflectance of the device increases to 0.57 for the maximum available THz field strength. This corresponds to a THz-induced absorption modulation of more than 3 orders of magnitude.

Furthermore, a slight red shift of resonance with increasing THz field strength is observed. In figure 40 (b) we observe also a significant phase modulation at frequencies around the resonance (region between dashed lines in figure b). We recorded an absolute THz-induced phase modulation of 130^{o}. This large phase modulation is responsible for the THz pulse reshaping when the THz field strength scales up. In order to exclude any nonlinearities induced by the intense THz fields on the ionic liquid substrate, we investigated separately a similar sample without the graphene layer and we did not observe any THz nonlinear response (see figure 41).

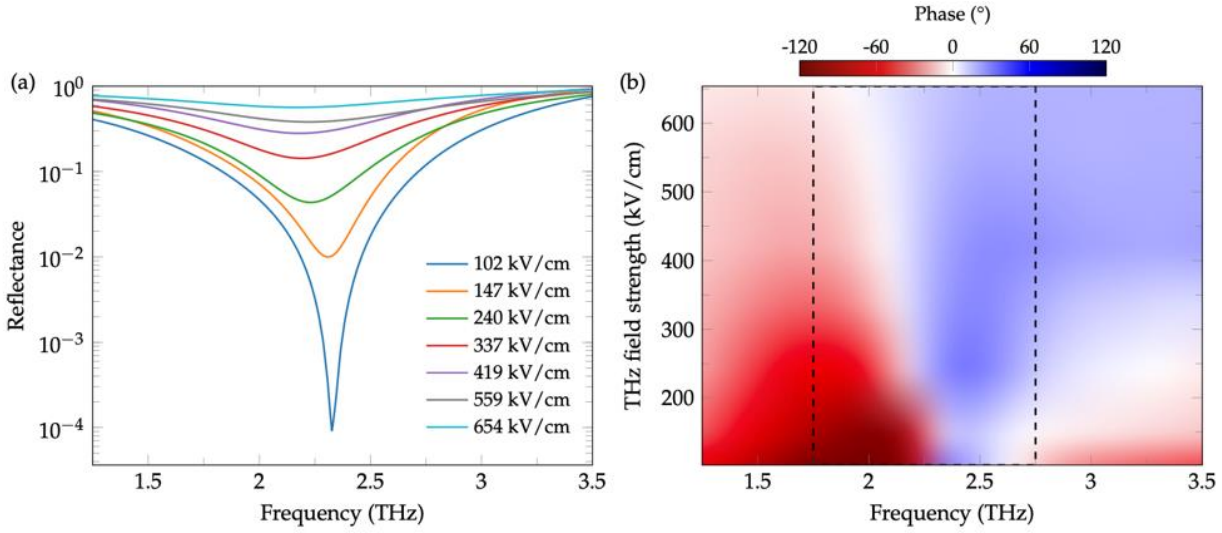

Figure 40: Experimentally measured reflectance (a) and phase (b) spectra for the cavity under various values of THz field strength in the range of 102-65 kV/cm. All spectra are normalized at the CNP

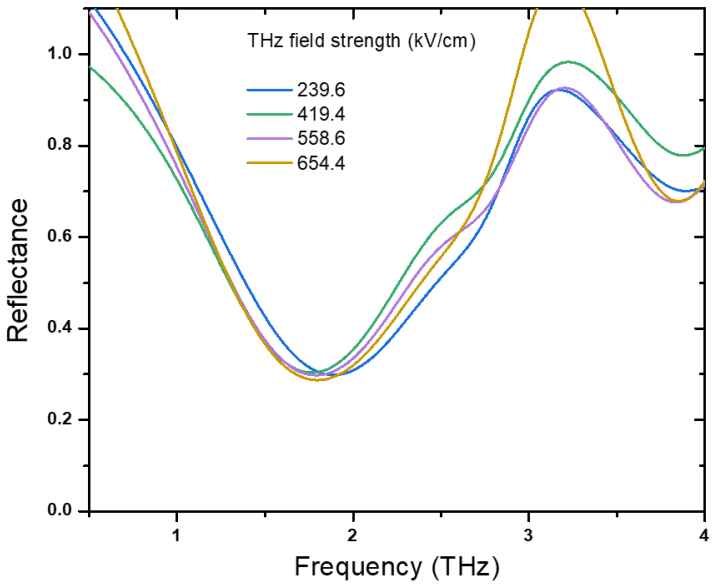

Figure 41: Experimentally measured reflectance of a sample without graphene layer

With the assistance of A. Tasolamprou and S. Doukas, we understand the origin of the observed nonlinear response performing a detailed modeling of the graphene's response to THz excitation. Figure 42 shows a schematic representation of this non-linear response. After the absorption of the incoming THz radiation, graphene carriers thermalize in an ultrafast time scale (~20 fs).[113,114]. Heat dissipation occurs in a much lower (~ps) time scale via emission of optical phonons [115,116] and disorder- assisted super collisions [117,118.] This leads to accumulation un the graphene carrier bath, raising the electronic temperature, T_e. The elevated T_e results in a reduced graphene chemical potential due to net carrier density conservation (i.e., n_e (μ, T_e) -n_h (μ, T_e) = const, where n_e (μ, T_e) and n_h (μ, T_e) are the graphene electron and hole densities, respectively and μ is the graphene chemical potential[119], and a broadened Fermi-Dirac distribution of graphene carriers. This reduces the intraband transitions, as explicitly evaluated by the Kubo formula[119] leading to a reduced intraband conductivity [120,121] and thus, to a reduced THz absorbance of graphene.

In order to quantitively describe the above graphene carrier and temperature dynamics are time integrated using a fourth- order Runge Kutta method (4RK)[119.] To do so we assume a two-temperature model [119,122]

$$c_e \frac{\partial T_e}{\partial t} = a_{SLG}(\omega, T_e) P_{in}(\omega, t) - J_{e-ph}(T_e, T_1) \quad (42)$$

$$c_1 \frac{\partial T_1}{\partial t} = J_{e-ph}(T_e, T_1) - \Gamma_{SLG-sub}(T_1 - T_{sub}) \quad (43)$$

where $\mathbf{c_e}$ and $\mathbf{c_l}$ are the electronic and lattice graphene thermal capacities, $\mathbf{T_e}$ and $\mathbf{T_l}$ are the graphene carrier lattice temperatures which are generally different, $\mathbf{a_{SLG}}$ **(ω, Te)** is the graphene absorption which depends on T_e and light frequency ω, $\boldsymbol{P_{in}}$ ***(ω, t)*** is the input power density of the THz source, $\mathbf{J_{e\text{-}ph}}$ **($\mathbf{T_e}$, $\mathbf{T_l}$)** is the thermal current density from the electron to the phonon bath, $\mathbf{\Gamma_{SLG-sub} \approx 20 MW\ m^{-2}K^{-1}}$ is the cooling rate of the graphene lattice into the substrate, and $\mathbf{T_{sub}}$ is the substrate temperature. However, it is discovered that the overall linear relationship with carrier energy occurs at the high Fermi levels (0.2 eV) and substrate supported graphene with low (10^4 cm^2/ (V s)) mobility utilized in our study. [120,123]. The description of conductivity variations caused by carrier heating has also been successfully applied using this linear scale. [100,121]

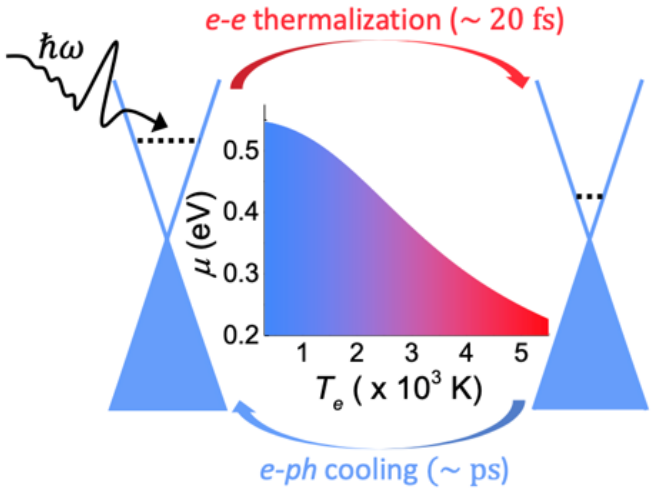

Figure 42: Schematic representation of graphene carriers upon heating following THz excitation

With the theoretical approaches, we observed a similar behavior with the experimental findings. Figure 43 (a) shows the reflectance spectra under different THz field strengths. As the THz field increases, so does the calculated reflectance presenting also the characteristic red shift of the resonance observed in the experiment. This absorption resonance is due to critical coupling of light into Fabry- Perot cavity formed by the graphene reflector and the back mirror and is sharper in theory compared to experiment. The latter is explained by inhomogeneous broadening caused by the substrate thickness and changes in graphene doping across the measuring spot size. At frequencies far from resonance, on the other hand, an antiresonance is expected, where the total reflection of the graphene-mirror system is larger than the reflection at CNP (where graphene is not reflecting) and thus normalized reflectance reaches above unity. This behavior is observed only in theoretical spectra due to the aforementioned inhomogeneous broadening. In figure 43 (b) we plot the minimum reflectance as a function of peak THz field strength, alongside the experimental results. Finally, is a good agreement between experiment and theory looking the final results for the resonance reflectance modulation.

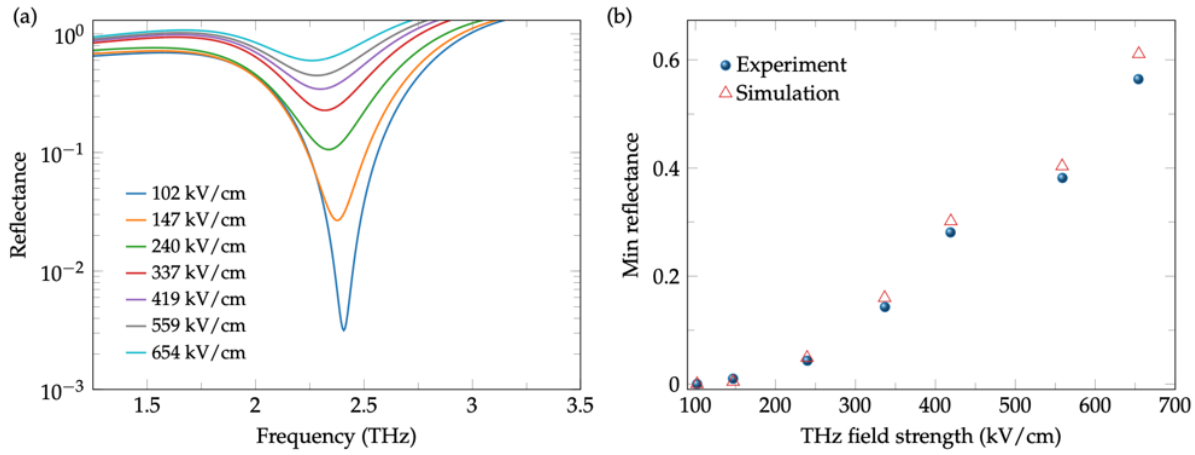

Figure 43: a) Reflectance spectra for different THz field strengths as calculated from our model. All spectra normalized at CNP b) Experimental and calculated minimum reflectance of the proposed device as a function of THz field strength

Finally, we can learn more about the carrier temporal dynamics during the THz excitation. Especially, in figure 44 (a), we can see the temporal evolution of carrier temperature during and shortly after the THz excitation. In figure 44 (b), we plot the respective temporal evolution of the real part of intraband conductivity (which is directly proportional to THz graphene absorbance) at the resonant frequency. This elucidates the near instantaneous thermalization of graphene carriers, in combination with their progressive cooling, leads to vanishing conductivity at higher THz field strengths. The latter is the source of the nonlinear absorption modulation observed in this work. Furthermore, we observe that the overall phenomenon occurs on the subps time scale, illustrating the ultrafast nature of the observed modulation.

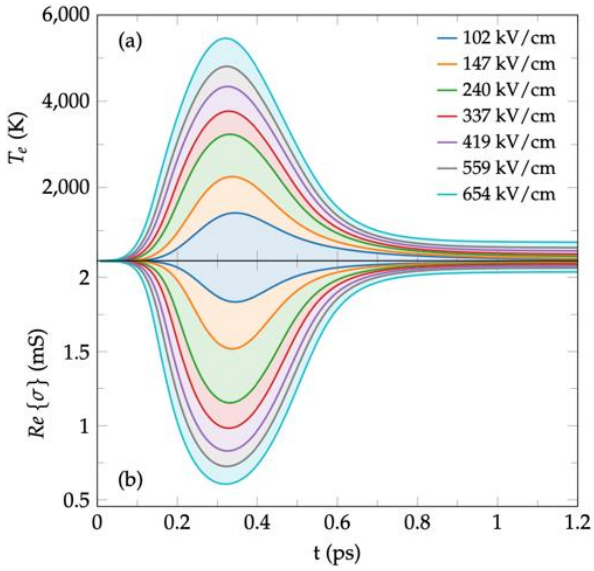

Figure 44: a) Calculated temporal evolution of (a) graphene carriers' temperature and (b) real part of intraband conductivity at the resonant frequency

7. Conclusions

In summary, in this work we demonstrated an electrically THz cavity with three different thicknesses by sandwiching a thick porous polyethylene membrane containing a room temperature ionic liquid electrolyte between graphene and a gold electrode. With this device configuration we measured directly the Fermi level under a bias voltage. First, we did measurements to identify the Fermi level with low and high-power THz sources. Perfect absorption was achieved only when using a low THz power source. Some of the results are comparable with those that have already been published, while others are presented in this work for the first time. So far, we have proved that our graphene-based Salisbury screen perfect absorbing device can be self-modulated in terms of its absorption properties. In our experiments, we observed an absorption modulation of more than 3 orders of magnitude and an absolute phase modulation of 130^{o} when the THz field scaled from 102 to 654 kV/cm. We have demonstrated that the irradiation of intense THz fields, results in heating of the graphene's carriers and a subsequent decrease of its chemical potential and intraband conductivity, while the phenomenon last less than a picosecond. These findings show a novel THz self-action-based mechanism for modifying the absorption and phase characteristics of graphene-based perfect absorbing device. Future dynamically modulated flat optics devices might use such technologies. Additionally, devices based on our work can be used to shape the beam and pulse of powerful THz emitters.

References

1. https://en.wikipedia.org/wiki/Electromagnetic_spectrum
2. https://commons.wikimedia.org/wiki/File:Thz_freq_in_EM_spectrum.png?uselang=en-gb
3. Taylor, R., Pratt, R. W. & Caldwell, B. D. Alternative approach to aeroservoelastic design and clearance. *IEE Proc. Control Theory Appl.* **143**, 1–8 (1996)
4. Zouaghi, W. *et al.* Broadband terahertz spectroscopy: Principles, fundamental research and potential for industrial applications. *Eur. J. Phys.* **34**, (2013)
5. Masayoshi Tonouchi, Cutting -edge terahertz technology, Nat.Photon, 1(2):**97**-105, (2007)
6. T. Globus, D. Woolard, M. Bykhovskaia, B. Gelmont, L. Werbos, and A. Samuels,"THz-frequency spectroscopic sensing of DNA and related biological materials," Int. J High Speed Electron. Syst., **13**, 903 (2003)
7. P. F. Taday, "Applications of terahertz spectroscopy to pharmaceutical sciences,"Phil. Trans. R. Soc. Lond. A, **362**, 351 (2004).
8. Hu, B.B & Nuss, M.C. Imaging with terahertz waves. *Opt. Lett*. **20**,1716(1995)
9. Ozyuner, L. et al. Emission of coherent THz radiation from superconductors. *Science* (80-.). **318**, 1291-1293 (2007)
10. Ghann, W.& Uddin, J. Terahertz Spectroscopy -A Cutting Edge Technology. Terahertz Spectrosc. - A Cut. Edge Technol. 3-20(2017)
11. A. A. Gowen, C. O'Sullivan, and C. P. O'Donnell, "Terahertz time domain spectroscopy and imaging: Emerging techniques for food process monitoring and quality control," Trends in Food Science & Technology **25**, 40-46 (2012).
12. Dandolo, et al. Inspection of panel paintings beneath gilded finishes using terahertz time-domain imaging. *Stud.Conserv*. **60**, S159-S166(2015)
13. Pawar, et al Terahertz technology and its applications. *Drug Invert. Today* **5**, 157-163(2013)
14. L. Hai-Bo, et al, Terahertz Spectroscopy and Imaging for Defense and Security Applications, *Proceedings of the Ieee* **95**, 1514-1527 (2007).
15. K. Kawase, et al, Non-destructive terahertz imaging of illicit drugs using spectral fingerprints, *Opt. Express* **11**, 2549-2554 (2003)
16. Prabira K.S et al, An Introduction to Terahertz Technology, Its History, Properties and Application, *Conf*. (2015)
17. Son et al, Potential clinical applications of terahertz radiation. *J. Appl.Phys*. **125**, (2019)
18. Jepsen et al, Terahertz spectroscopy and imaging- Modern techniques and applications. *Laser Photonics Rev*. **5** ,124-166 (2011)
19. Baxter et al. Terahertz spectroscopy. *Anal. Chem.* **83**, 4342-4368(2011)
20. X.-C. a. J. X. Zhang, *Introduction to THz Wave Photonics* (2010)
21. Mickan et al. "T-ray sensing and imaging", *International Journal of High-Speed Electronics and Systems*, **13(2),** 601-676 (2003)

22. Darrow et al, "Power scaling of large-aperture photoconducting antennas," Applied Physics Letters **58**, 25-27 (1991)
23. N. Bloembergen, Nonlinear Optics, 4th edition, (Benjamin Inc. 1965).
24. https://en.wikipedia.org/wiki/Optical_rectification
25. C.O Sullivan J and A. Murphy, *Terahertz Sources, Detectors, and Optics*
26. K.Reimann, Table-top sources of ultrashort THz pulses ,*Rep. Prog. Phys.***70** 1597 (2007)
27. X.-C. a. J. X. Zhang, *Introduction to THz Wave Photonics* (2010)
28. A. A. Gowen, C. O'Sullivan, and C. P. O'Donnell, "Terahertz time domain spectroscopy and imaging: Emerging techniques for food process monitoring and quality control," Trends in Food Science & Technology **25**, 40-46 (2012).
29. A.Koulouklidis, Intense Broadband THz Fields from Laser- Plasma Interactions , PhD
30. N.Nemoto et al. "Highly precise and accurate terahertz polarization measurements based on electro-optic sampling with polarization modulation of probe pulses," Opt. Express **22**, 17915-17929 (2014)
31. N.Karpowicz et all "Coherent heterodyne time-domain spectrometry covering the entire terahertz gap", Appl.Phys.Lett.92, 011131(2018)
32. P.L.Kelley ,Self-focusing of optical beams, Phys.Rev.Lett.15
33. L.Gallmann et al. "Photoemission and photoionization time delays and rates", Structural Dynamics 4 (2017)
34. R.Wang et al. "Identification of tunneling and multiphoton ionization in intermediate Keldysh parameter regime" Opt.Exp, vol.27 ,no. 5(2019)
35. https://fr.wikipedia.org/wiki/Filamentation_laser
36. J.Li et al, "Generation of Ultrabroad and intense Supercontinuum in Mixed Multiple Thin Plates", Photonics 2021,**8**,311
37. A.Schmitt-Sody et al. "Picosecond laser filamentation in air". New.J.Phys.18 (2016)
38. Koulouklidis, A.D., Gollner, C., Shumakova, V. *et al*. Observation of extremely efficient terahertz generation from mid-infrared two-color laser filaments. *Nat Commun* **11**, 292 (2020)
39. Fedorov and Tzortzakis "Powerful terahertz waves from long-wavelength infrared laser filaments" , Light: Science &Applications (2020) 9:186
40. X.Xie et al, "Coherent Control of THz Wave Generation in Ambient Air", PRL 96(2006)
41. K.-Y. Kim et al.,"Terahertz emission from ultrafast ionizing air in symmetry-broken laser fields," Opt. Express **15**, 4577-4584 (2007).
42. C.Kubler et al., Ultrabroadband terahertz pulses: generation and field-resolved detection. Semiconductor Science and Technology, (7): S128,2005
43. S. Casalbuoni, et al, "Numerical studies on the electro-optic detection of femtosecond electron bunches," Physical Review Special Topics - Accelerators and Beams **11**, 072802 (2008).

44. https://www.toptica.com/fileadmin/Editors_English/11_brochures_datasheets/01_brochures/toptica_BR_Terahertz_Technologies.pdf
45. Susan L. Dexheimer, Terahertz Spectroscopy, principles and applications CRC Press, December 2017
46. Kai-Erik Peiponem, Axel Zeitler and Makoto Kuwata- Gonokami, Terahertz spectroscopy and imaging, Springer series in optical Sciences, 2013
47. A. Geim and K. Novoselov, The rise of graphene, Nature materials, 2007 183–191**(2007)**
48. Daniel R. Cooper et al, "Experimental review of graphene"
49. Rafael et al, Theory of 2D crystals: graphene and beyond, **Chem. Soc. Rev., 2017,** 46**, 4387-4399**
50. T.Puiu , "Graphene layered in 3D crystal structure might allow for electronics revolution" , Nanotechnology Research , 2012
51. Hassan A. Hafez, Sergey Kovalev, Klaas-Jan Tielrooij, Mischa Bonn, Michael Gensch, Dmitry Turchinovich , Terahertz Nonlinear Optics of Graphene: From Saturable Absorption to High-Harmonics Generation , Adv.Optic.Materials , 2019
52. Wei Chen, Xin Dong, Yan Xu, Yang Gao, Xiaoqiang Sun, Daming Zhang, Broadband graphene modulator with high modulation depth based on tip plasmonic waveguide ,2022
53. Hassan A. Hafez, Ibraheem Al-Naib, Marc M. Dignam, Yoshiaki Sekine, Katsuya Oguri, François Blanchard, David G. Cooke, Satoru Tanaka, Fumio Komori, Hiroki Hibino, and Tsuneyuki Ozaki, Nonlinear terahertz field-induced carrier dynamics in photoexcited epitaxial monolayer graphene, Phys. Rev. B 91, 035422, 2015
54. A. R. Wright, X. G. Xu, J. C. Cao, *and* C. Zhang,Strong nonlinear optical response of graphene in the terahertz regime, Appl. Phys. Lett. **95**, 072101 (2009)
55. P.A.Obraztsov, M.G.Rybin, A.V.Tyurnina, S.V.Garvon, E.D.Obraztsova, A.N.Obraztsov and Y.D.Svivko, Broadband light-induced absorbance change in multilayer graphene, Nano letters,11(4):15140-1545 2011
56. Mikhailov, Sergey A. and Klaus Ziegler. "Nonlinear electromagnetic response of graphene: frequency multiplication and the self-consistent-field effects." Journal of Physics: Condensed Matter 20 (2008): 384204.
57. K.L.Ishikawa , Nonlinear optical response of graphene in time domain Phys, Rev.B 82, 201402, 2010
58. M J Paul, Y C Chang, Z J Thompson, A Stickel, J Wardini, H Choi, E D Minot, B Hou, J A Nees, T B Norris, High-field terahertz response of graphene, *New J. Phys.* **15** 085019, 2013
59. T.Elsaesser, K.Reimann, M.Werner, Extremely efficient terahertz high-harmonic generation in graphene by hot Dirac fermions, concepts and Applications of Nonlinear Terahertz spectroscopy, 2019
60. Winnerl S, Orlita M, Plochocka P, Kossacki P, Potemski M, Winzer T, Malic E, Knorr A, Sprinkle M, Berger C, de Heer WA, Schneider H, Helm M. Carrier relaxation in epitaxial graphene photoexcited near the Dirac point. Phys Rev Lett. 2011.

61. Wang F, Zhang Y, Tian C, Girit C, Zettl A, Crommie M, Shen YR. Gate-variable optical transitions in graphene. Science. 2008 Apr 11;320(5873):206-9, Epub 2008
62. Gan X, Shiue RJ, Gao Y, Mak KF, Yao X, Li L, Szep A, Walker D Jr, Hone J, Heinz TF, Englund D. High-contrast electrooptic modulation of a photonic crystal nanocavity by electrical gating of graphene. Nano Lett. 2013 Feb 13;13(2):691-6. Epub 2013
63. Li, Z., Henriksen, E., Jiang, Z. *et al.* Dirac charge dynamics in graphene by infrared spectroscopy. *Nature Phys* **4**, 532–535 (2008)
64. Kin Fai Mak, Long Ju, Feng Wang, Tony F. Heinz, Optical spectroscopy of graphene: From the far infrared to the ultraviolet, Solid-State Communications, 2012
65. S. Das Sarma, Shaffique Adam, E. H. Hwang, and Enrico Rossi**,** Electronic transport in two-dimensional graphene Rev. Mod. Phys. 83, **407,** 2011
66. Des Wang L, An N, He X, Zhang X, Zhu A, Yao B, Zhang Y. Dynamic and Active THz Graphene Metamaterial Devices. Nanomaterials (Basel). 2022 17;12(12):2097.
67. Liaskos, C., Tsioliaridou, A., Pitsillides, A., Akyildiz, I. F., Kantartzis, N. V., Lalas, A. X., Dimitropoulos, X., Ioannidis, S., Kafesaki, M., & Soukoulis, C. M. (2015). Design and Development of Software Defined Metamaterials for Nanonetworks. *IEEE CIRCUITS AND SYSTEMS MAGAZINE*, *15*(4), 12-25
68. I. F. Akyildiz, A. Kak and S. Nie, "6G and Beyond: The Future of Wireless Communications Systems," in *IEEE Access*, vol. 8, pp. 133995-134030, 2020
69. Z.T.Ma, Z.X.Geng, Z.XFan,J.Liu and H.D.Chen, Modulators for Terahertz Communication: The current state of the art, AAAS, 2019
70. T. Vogel, G. Dodel, E. Holzhauer, H. Salzmann, and A. Theurer.High-speed switching of far-infrared radiation by photoionization in a semiconductor.Applied Optics,31(3):329–337,January 1992
71. Tatsuo Nozokido, Hiroaki Minamide, and Koji Mizuno.Modulation of submillimeter wave radiation by laserproduced free carriers in semiconductors.Electronics and Communications in Japan (Part II: Electronics),80(6):1–9, June 1997.
72. Hou-Tong Chen, Willie J. Padilla, Joshua M. O. Zide,Arthur C. Gossard, Antoinette J. Taylor, and Richard D. Averitt.Active terahertz metamaterial devices.Nature,444(7119):597–600, November 2006
73. Rusen Yan, Berardi Sensale-Rodriguez, Lei Liu, Debdeep Jena, and Huili Grace Xing, "A new class of electrically tunable metamaterial terahertz modulators," Opt. Express **20**, 28664-28671 (2012)
74. J. Gmez Rivas, M. Kuttge, H. Kurz, P. Haring Bolivar, and J. A. Snchez-Gil.Low-frequency active surface plasmon optics on semiconductors. Applied Physics Letters,88(8):082106, February2006,
75. T. Driscoll, S. Palit, M. M. Qazilbash, M. Brehm, F. Keil-mann, Byung-Gyu Chae, Sun-Jin Yun, Hyun-Tak Kim, S. Y.Cho, N. Marie Jokerst, D. R. Smith, and D. N. Basov.Dynamic tuning of an infrared hybrid-metamaterial resonance using vanadium dioxide.Applied Physics Letters,93(2):024101, July2008

76. J. Gmez Rivas, M. Kuttge, H. Kurz, P. Haring Bolivar, and J. A. Snchez-Gil.Low-frequency active surface plasmon optics on semiconductors.Applied Physics Letters,88(8):082106, February 2006
77. J.Valentine, S.Zhang, T.Zentgraf, A.E.Ulin, D.A.Genov, G.Bartal, Three-dimensional optical metamaterial with a negative refractive index (2008)., Nature, 455(7211), pp. 376–379
78. https://en.wikipedia.org/wiki/Electromagnetic_metasurface
79. Y.Cheng, W.Withayachumnakul, A.Upadhyay, D.Headland, Y.Nie, R.Gong, M.Bhaskaran, A.Sriram and D.Abbott, Ultrabroadband plasmonic absorber for terahertz waves, Advanced Optical Materials, (2015), 3(3), pp. 376–380.
80. C.M.Watts,X.Liu and W.J.Padilla Metamaterial electromagnetic wave absorbers, (2012). Advanced Materials, 24(23)
81. Zhaoxian Su, Jianbo Yin, and Xiaopeng Zhao, "Terahertz dual-band metamaterial absorber based on graphene/MgF_2 multilayer structures," Opt. Express **23**, 1679-1690 (2015)
82. Ying Zhang, Yan Shi, and Chang-Hong Liang, "Broadband tunable graphene-based metamaterial absorber," Opt. Mater. Express **6**, 3036-3044 (2016)
83. Liu, Z.; Guo, L.; Zhang, Q. A Simple and Efficient Method for Designing Broadband Terahertz Absorber Based on Singular Graphene Metasurface. *Nanomaterials* **2019**, *9*, 1351.
84. R. Alaee et al, "Theory of metasurface based perfect absorbers", Journal of physics D: Applied Physics, 2017
85. J.M. Woo et al, "Graphene based Salisbury screen for terahertz absorber", Applied physics letters 104,081106(2014)
86. Admin Asrmeta, "Early accounts of perfect light absorbers to absorb electromagnetic waves
87. T.Badloe et al , "Metasurfaces -Based Absorption and Reflection Control: Perfect Absorbers and Reflectors" , Journal of Nanomaterials ,vol.2361042, (2017)
88. Mehdi, I.; Siles, J. V.; Lee, C.; Schlecht, E. THz Diode Technology: Status, Prospects, and Applications. Proceedings of the IEEE 2017, 105, 990–1007
89. Jeong, Y.-G.; Bahk, Y.-M.; Kim, D.-S. Dynamic Terahertz Plasmonics Enabled by Phase-Change Materials. Advanced Optical Materials 2020, 8
90. Rahm, M.; Li, J.-S.; Padilla, W. J. THz Wave Modulators: A Brief Review on Different Modulation Techniques. 2013, 34, 1–27
91. J.M.Kroon et al ,Electrical and optical properties of graphene -TiO_2 nanocomposite and its applications in dye sensitized solar cells , Prog. Photovoltaics 15(2007), 1-18.
92. Ferrari, A. et al. Science and technology roadmap for graphene, related two-dimensional crystals, and hybrid systems. Nanoscale 2015, 7, 4598–4810
93. Mittendorff, M.; Li, S.; Murphy, T. E. Graphene-Based Waveguide-Integrated Terahertz Modulator. ACS Photonics 2017, 4, 316–321.

94. Castilla, S.; Terr´es, B.; Autore, M.; Viti, L.; Li, J.; Nikitin, A. Y.; Vangelidis, I.; Watanabe, K.; Taniguchi, T.; Lidorikis, E.; Vitiello, M. S.; Hillenbrand, R.; Tielrooij, K.-J.; Koppens, F. H. Fast and Sensitive Terahertz Detection Using an Antenna-Integrated Graphene pn Junction. Nano Letters 2019, 19, 2765–2773
95. Pendry, J.; Huidobro, P.; Silveirinha, M.; Galiffi, E. Crossing the light line. Nanophotonics 2022 ,11, 161-167
96. Shaltout, A.; Shalaev, V.; Brongersma, M. Spatiotemporal light control with active metasurfaces. Science 2019, 364
97. Malevich, Y.; Ergoktas, M. S.; Bakan, G.; Steiner, P.; Kocabas, C. Video-Speed Graphene Modulator Arrays for Terahertz Imaging Applications. ACS Photonics 2020, 7, 2374–2380
98. Doukas, S.; Chatzilari, A.; Dagkli, A.; Papagiannopoulos, A.; Lidorikis, E. Deep and fast free-space electro-absorption modulation in a mobility-independent graphene-loaded Bragg resonator. Applied Physics Letters 2018, 113, 011102.
99. Jeong Min Woo, Min-Sik Kim, Hyun Woong Kim, *and* Jae-Hyung Jang. Graphene based Salisbury screen for terahertz absorber. Applied Physics Letters 2014, 104, 081106
100. Tasolamprou, A. C.; Koulouklidis, A. D.; Daskalaki, C.; Mavidis, C. P.; Kenanakis, G.; Deligeorgis, G.; Viskadourakis, Z.; Kuzhir, P.; Tzortzakis, S.; Kafesaki, M.; Economou, E. N.; Soukoulis, C. M. Experimental Demonstration of Ultrafast THz Modulation in a Graphene-Based Thin Film Absorber through Negative Photoinduced Conductivity. ACS Photonics 2019, 6, 720–727.
101. Hafez, H. A.; Kovalev, S.; Tielrooij, K.-J.; Bonn, M.; Gensch, M.; Turchinovich, D. Terahertz nonlinear optics of graphene: from saturable absorption to high-harmonics generation. Advanced Optical Materials 2020, 8, 1900771.
102. Koulouklidis, A. D.; Gollner, C.; Shumakova, V.; Fedorov, V. Y.; Pugˇzlys, A.; Baltuˇska, A.; Tzortzakis, S. Observation of extremely efficient terahertz generation from mid-infrared two-color laser filaments. Nature Communications 2020,11,292.
103. Shalaby, M.; Hauri, C. P. Demonstration of a low-frequency three-dimensional terahertz bullet with extreme brightness. Nature Communications 2015, 6, 5976, Number: 1 Publisher: Nature Publishing Group
104. Dey, I.; Jana, K.; Fedorov, V. Y.; Koulouklidis, A. D.; Mondal, A.; Shaikh, M.; Sarkar, D.; Lad, A. D.; Tzortzakis, S.; Couairon, A.; Kumar, G. R. Highly efficient broadband terahertz generation from ultrashort laser filamentation in liquids. Nature communications 2017, 8,1184
105. Jadidi, M. M. Konig-Otto, J. C.; Winnerl, S.; Sushkov, A. B.; Drew, H. D.; Murphy, T. E.; Mittendor, M. Nonlinear Terahertz Absorption of Graphene Plasmons. Nano Letters 2016, 16, 2734–2738
106. Z. T. Ma, Z. X. Geng, Z. Y. Fan, J. Liu, H. D. Chen, "Modulators for Terahertz Communication: The Current State of the Art", *Research*, vol. 2019, Article ID 6482975, 22 pages, 2019

107. Kakenov, Nurbek, et al. "Observation of gate-tunable coherent perfect absorption of terahertz radiation in graphene." *Acs Photonics* 3.9 (2016): 1531-1535.
108. Anna C. Tasolamprou, Anastasios D. Koulouklidis, Christina Daskalaki, Charalampos P. Mavidis, George Kenanakis, George Deligeorgis, Zacharias Viskadourakis, Polina Kuzhir, Stelios Tzortzakis, Maria Kafesaki, Eleftherios N. Economou, Costas M. Soukoulis. Experimental Demonstration of Ultrafast THz Modulation in a Graphene-Based Thin Film Absorber through Negative Photoinduced Conductivity. ACS Photonics **2019,** *6* (3) , 720-727.
109. Anastasios D. Koulouklidis, Anna C. Tasolamprou, Spyros Doukas, Eudokia Kyriakou, M. Said Ergoktas, Christina Daskalaki, Eleftherios N. Economou, Coskun Kocabas, Elefterios Lidorikis, Maria Kafesaki, Stelios Tzortzakis. Ultrafast Terahertz Self-Induced Absorption and Phase Modulation on a Graphene-Based Thin Film Absorber. ACS Photonics **2022,** *9* (9), 3075-3082.
110. Koulouklidis, A. D.; Fedorov, V. Y.; Tzortzakis, S. Spectral bandwidth scaling laws and reconstruction of THz wave packets generated from two-color laser plasma filaments. Physical Review A 2016, 93, 033844.
111. Liu, F. L.; Chong, Y. D.; Adam, S.; Polini, M. Gate-tunable coherent perfect absorption of terahertz radiation in graphene. 2D Mater. 2014, 1, 031001.
112. Fan, Y. C.; Zhang, F. L.; Zhao, Q.; Wei, Z. Y.; Li, H. Q. Tunable terahertz coherent perfect absorption in a monolayer graphene. Opt. Lett. 2014, 39, 6269−6272
113. . Yi Z, Chen J, Cen C, Chen X, Zhou Z, Tang Y, Ye X, Xiao S, Luo W, Wu P. Tunable Graphene-based Plasmonic Perfect Metamaterial Absorber in the THz Region. Micromachines (Basel). 2019 Mar 18;10(3):194.
114. Tomadin, A.; Brida, D.; Cerullo, G.; Ferrari, A. C.; Polini, M. Nonequilibrium dynamics of photoexcited electrons in graphene: Collinear scattering, Auger processes, and the impact of screening. *Phys. Rev. B* 2013, *88*, 035430
115. Brida, D.; Tomadin, A.; Manzoni, C.; Kim, Y. J.; Lombardo, A.; Milana, S.; Nair, R. R.; Novoselov, K. S.; Ferrari, A. C.; Cerullo, G.; Polini, M. Ultrafast collinear scattering and carrier multiplication in graphene. *Nat. Commun.* 2013, *4*, 1−9
116. Pogna, E. A.; Jia, X.; Principi, A.; Block, A.; Banszerus, L.; Zhang, J.; Liu, X.; Sohier, T.; Forti, S.; Soundarapandian, K.; et al. Hot-Carrier Cooling in High-Quality Graphene Is IntrinsicallyLimited by Optical Phonons. *ACS Nano* 2021, *15*, 11285−11295.
117. Viljas, J.; Heikkila, T. Electron-phonon heat transfer in monolayer and bilayer graphene. *Phys. Rev. B* 2010, *81*, 245404
118. Song, J. C.; Reizer, M. Y.; Levitov, L. S. Disorder-assisted electron-phonon scattering and cooling pathways in graphene. *Physical review letters* 2012, *109*, 106602.
119. Song, J. C.; Levitov, L. S. Energy flows in graphene: hot carrier dynamics and cooling. *J. Phys.: Condens. Matter* 2015, *27*, 164201
120. Doukas, S.; Mensz, P.; Myoung, N.; Ferrari, A. C.; Goykhman, I.; Lidorikis, E. Thermionic graphene/silicon Schottky infrared photodetectors. *Phys. Rev. B* 2022, *105*, 115417

121. Tielrooij, K.-J.; Song, J.; Jensen, S. A.; Centeno, A.; Pesquera,A.; Zurutuza Elorza, A.; Bonn, M.; Levitov, L.; Koppens, F. Photoexcitation cascade and multiple hot-carrier generation in graphene. *Nat. Phys.* 2013, *9*, 248−252

122. Mics, Z.; Tielrooij, K.-J.; Parvez, K.; Jensen, S. A.; Ivanov, I.; Feng, X.; Müllen, K.; Bonn, M.; Turchinovich, D. Thermodynamic picture of ultrafast charge transport in graphene. *Nat. Commun.* 2015, *6*, 1−7

123. Massicotte, M.; Schmidt, P.; Vialla, F.; Watanabe, K.; 596 Taniguchi, T.; Tielrooij, K.-J.; Koppens, F. H. Photo-thermionic effect in vertical graphene heterostructures. *Nat. Commun.* 2016, *7*, 1−7

124. Massicotte, M.; Soavi, G.; Principi, A.; Tielrooij, K.-J. Hot carriers in graphene−fundamentals and applications. *Nanoscale* 2021,*13*, 8376−8411